

Palomar/Las Campanas Imaging Atlas of Blue Compact Dwarf Galaxies: I. Images and Integrated Photometry

A. Gil de Paz^{1,2,3}, B. F. Madore^{1,3}, and O. Pevunova¹

ABSTRACT

We present B , R , and $H\alpha$ images for a total of 114 nearby galaxies ($v_{\text{helio}} < 4000 \text{ km s}^{-1}$) that, with exception of 9 objects, are classified as Blue Compact Dwarfs (BCDs). BR integrated magnitudes, $H\alpha$ fluxes and $H\alpha$ equivalent widths for all the objects in the sample are presented. A new set of quantitative, observational criteria for a galaxy to be classified as a BCD is proposed. These criteria include a limit on the K -band luminosity (i.e. stellar mass; $M_K > -21 \text{ mag}$), peak surface brightness ($\mu_{B,\text{peak}} < 22 \text{ mag/arcsec}^2$), and color at the peak surface brightness ($\mu_{B,\text{peak}} - \mu_{R,\text{peak}} \lesssim 1$). $H\alpha$ emission is detected in all but three sample galaxies. Typical color, absolute magnitude, and $H\alpha$ luminosity are $(B - R) = 0.7 \pm 0.3 \text{ mag}$, $M_B = -16.1 \pm 1.4 \text{ mag}$, and $\log(L_{H\alpha}) = 40.0 \pm 0.6 \text{ (erg s}^{-1}\text{)}$. Galaxies morphologically classified as nE and iE BCDs within our sample show lower $H\alpha$ equivalent widths and redder colors, on average, than the iI and i0-type BCDs. For most of the galaxies the presence of an evolved stellar population is required to explain their observed properties; only the most metal-poor BCDs (e.g. I Zw 18, Tol 65) are still compatible with a pure, young burst. The flux-calibrated and WCS-compliant images in this Atlas are individually available through the NASA/IPAC Extragalactic Database (NED) image server and collectively through a dedicated web page at (http://nedwww.ipac.caltech.edu/level5/Sept02/Palco_BCD/frames.html).

Subject headings: galaxies: evolution — galaxies: starburst — galaxies: dwarf — galaxies: fundamental parameters — galaxies: photometry — atlases

¹NASA/IPAC Extragalactic Database, California Institute of Technology, MS 100-22, Pasadena, CA 91125; agpaz, barry, olga@ipac.caltech.edu

²Jet Propulsion Laboratory, California Institute of Technology, MS 183-900, Pasadena, CA 91109

³The Observatories, Carnegie Institution of Washington, 813 Santa Barbara Street, Pasadena, CA 91101

1. Introduction

Dwarf galaxies play a crucial role in contemporary theories for the formation and evolution of galaxies. They are proposed to be the building blocks from which larger systems have been created by merging (Kauffmann, White, & Guiderdoni 1993).

Blue Compact Dwarf galaxies (BCDs) are spectroscopically characterized by a faint, blue optical continuum accompanied, in most cases, by intense emission lines. Their current star formation rates (Fanelli et al. 1988) and neutral gas content (Thuan & Martin 1981) imply gas consumption time-scales of $\sim 10^9$ yr, much shorter than the age of the Universe. This fact, combined with the low metal abundances ($1/3 > Z > 1/50 Z_{\odot}$; Hunter and Hoffman 1999), led Searle, Sargent, & Bagnuolo (1973) to suggest earlier that either these objects are young galaxies or that they have experienced an episodic star-formation history.

The analysis of BCD surface brightness and color profiles (James 1994; Papaderos et al. 1996a,b; Doublier et al. 1997, 1999; Cairós et al. 2001a,b) combined with *HST* color-magnitude diagrams (Aloisi, Tosi, & Greggio 1999; Schulte-Ladbeck et al. 1999, 2000, 2001; Östlin 2000; Crone et al. 2000, 2002; Drozdovsky et al. 2001) has shown the existence of an underlying stellar population at least a few 10^9 yr old in most of these galaxies, i.e. these are not purely “young” galaxies. In this sense, Legrand et al. (2000) and Crone et al. (2000) have recently suggested that the formation of this evolved stellar population could have taken place at a low but continuous rate rather than in a purely bursting mode (see also Heller et al. 2000 concerning the lack of other evidence for random star formation in BCDs). Only in the case of the most metal poor BCDs ($Z < 1/20 Z_{\odot}$; Izotov & Thuan 1999) are the results regarding their evolutionary status still contradictory, mainly due to uncertain distances (Östlin 2000) and contamination of the galaxy outer halo colors by nebular emission (Izotov et al. 2001a,b; Papaderos et al. 1998, 2002).

Understanding of the role played by the collective supernovae-driven winds in the mass (i.e. luminosity) and chemical evolution, and in the propagation of the star formation in these galaxies is also mandatory. In this sense, the evolution of these winds in low-mass galaxies like the BCDs is thought to lead to the loss of a (still highly uncertain) fraction of metals (De Young & Heckman 1994; Mac-Low & Ferrara 1999; Silich & Tenorio-Tagle 2001), making these galaxies arguably one of the major polluters of the intergalactic medium (Ferrara & Tolstoy 2000).

In order to shed light on some of these questions we have obtained *BRH α* imaging data for a statistically significant sample of BCD galaxies. This sample includes 114 galaxies, 105 of them classified as BCDs. Similar recent studies include Papaderos et al. (1996a,b), Telles & Terlevich (1997), Doublier et al. (1997, 1999), and Cairós et al. (2001a,b). However, these

studies analyze samples that contain at least a factor of 4 fewer galaxies than our sample and, excepting the recent work of Cairós et al. (2001b), none of these studies include emission-line imaging data.

In Section 2 we describe the properties of our sample. A new set of observational, quantitative criteria to define the Blue Compact Dwarf class of galaxies is proposed in Section 3. The observations and reduction procedures are described in Sections 4 and 5. Sections 6 and 7 present the images of the galaxies along with their morphological classification. The results from the analysis of the integrated photometry of the sample are given in Section 8. We summarize our conclusions in Section 9. In Paper II we will analyze the structural properties of the sample, both in the continuum and in the emission-lines, by carrying out a decomposition of the surface brightness profiles, and presenting the concentration and asymmetry parameters in the different bands.

2. Sample

The galaxies in our sample have been selected from several exploratory studies including the Markarian lists (Mrk – Markarian, Lipovetskii, & Stepanian 1981), Second Byurakan (SBS – Markarian, Stepanian, & Erastova 1986), University of Michigan (UM – MacAlpine & Williams 1981), Palomar Objective-prism X (POX – Kunth, Sargent, & Kowal 1981), Hamburg/SAO (HS – Ugryumov et al. 1999), Universidad Complutense de Madrid (UCM – Zamorano et al. 1994, 1996; Alonso et al. 1999), and Tololo (Tol – Smith, Aguirre, & Zemelan 1976) surveys, as well as the lists of Zwicky & Zwicky (1971), and Haro (1956). Mrk and SBS galaxies were originally selected by their ultraviolet excess on photographic plates taken with the objective-prism technique. POX, HS, UM, UCM, & Tol galaxies were discovered by the presence of emission lines, [OIII] λ 5007Å (UM, HS, & Tol), H α (UCM), or both (POX), in objective-prism spectra. Finally, galaxies in the lists of Zwicky & Zwicky (1971) and Haro (1956) were selected according to their compactness and blue colors as inferred from photographic plates taken through 3 different filters (blue, red, & infrared).

From the list of BCD galaxies discovered in these surveys we have selected objects with heliocentric recession velocities lower than 4000 km s⁻¹. This limit was set by the longest-wavelength H α filter (PO 6640) available within the Palomar Observatory narrow-band filters set. Our sample also includes the six Virgo Cluster BCDs analyzed by Popescu et al. (2002) and the highly obscured Local Group galaxy IC 10. Although this latter galaxy has been ordinarily classified as a dwarf irregular, the recent study of Richer et al. (2001) shows that its structural properties resemble more those of BCD galaxies (see Papaderos et al. 1996a).

Our final sample consists of 114 galaxies.

It is worth mentioning that this sample does not include all the galaxies classified as BCDs in those surveys (noteworthy missing objects are UM 461, UM 462, or UM 465). Our sample cannot either be considered a complete sample since it has been selected from surveys that used different techniques and, therefore, are affected by different selection criteria.

In Table 1 we summarize the basic properties of the galaxies in this Atlas. In the few cases where the distance to the galaxy had been determined by measuring the magnitude of the tip of the RGB we adopted the distance value given by this method (see Lee, Freedman, & Madore 1993). In the vast majority of the cases we computed the distance using the Galactic Standard of Rest velocity of the galaxies assuming a Hubble constant of $70 \text{ km s}^{-1} \text{ Mpc}^{-1}$ (Freedman et al. 2001). Distances to the galaxies in the Virgo Cluster were adopted to be 16 Mpc (Macri et al. 1999). For 49 galaxies with published data the $[\text{NII}]\lambda 6584\text{\AA}/\text{H}\alpha$ line ratios required to correct the $\text{H}\alpha$ fluxes measured from the $[\text{NII}]\lambda\lambda 6548, 6584\text{\AA}$ doublet contamination were taken from Guseva, Izotov, & Thuan (2000), Izotov & Thuan (1999), Terlevich et al. (1991), Kennicutt (1992), Vílchez (1995), Masegosa, Moles, & Campos-Aguilar (1994), Kobulnicky & Skillman (1998), Kniazev et al. (201), van Zee et al. (1998a), Hunter & Hoffman (1999), Steel et al. (1996), Vacca & Conti (1992), Thuan, Izotov, & Lipovetsky (1995), Popescu & Hopp (2000), Garnett (1990), Thuan, Izotov, & Foltz (1999), Jansen et al. (2000), Rego et al. (1998), and Augarde et al. (1990). In those cases where the $[\text{NII}]\lambda 6584\text{\AA}/\text{H}\alpha$ line ratio was not available we adopted an average value of 0.055 computed using the 49 galaxies in our sample that do have $[\text{NII}]\lambda 6584\text{\AA}/\text{H}\alpha$ data. For comparison the average value obtained by Hunter & Hoffman (1999) for the BCDs in their sample was 0.091.

Equatorial coordinates, Galactic extinction (A_B) and heliocentric radial velocity values for the sample were taken from NED (see Table 1). Galactic extinction data are derived from the $100 \mu\text{m}$ maps of Schlegel, Finkbeiner, & Davis (1998). The values obtained are typically smaller than $A_B=0.5 \text{ mag}$, except for IC 10 (6.2 mag), II Zw 40 (3.5 mag), and NGC 2915 (1.2 mag). In the case of IC 10 the very low Galactic latitude makes the foreground extinction correction very uncertain.

3. Definition of Blue Compact Dwarf galaxy

In the past many different criteria have been used to classify a galaxy as a BCD or not. These criteria were commonly based on the galaxy’s luminosity and its morphological properties (Zwicky & Zwicky 1971; Thuan & Martin 1981) although definitions based on their spectroscopic properties are also found in the literature (Gallego et al. 1996). Moreover,

galaxies morphologically classified as BCDs are sometimes confused with spectroscopically-classified objects, such as “isolated extragalactic HII regions” (Sargent & Searle 1970), “HII galaxies” (Terlevich et al. 1991) or “Sargent-Searle objects” (SS; Salzer, MacAlpine, & Borson 1989). For instance, although the “isolated extragalactic HII regions” of Sargent & Searle (1970) and SS objects of Salzer et al. (1989) can be undoubtedly classified as BCDs, many HII galaxies in Terlevich et al. (1991) are significantly brighter than a BCD.

The original definition of “Compact Galaxy” comes from Zwicky (1970) where he defined as “compact” any galaxy (or any part of a galaxy) whose surface brightness is brighter than 20 mag/arcsec^2 in any chosen wavelength range. The term “blue”, as used by Zwicky, refers to those galaxies satisfying the previous condition on both blue and red plates (Zwicky & Zwicky 1971). Later on, Thuan & Martin (1981) introduced the term “Blue Compact Dwarf” referring to those galaxies having absolute blue magnitudes fainter than $M_B = -18.15 \text{ mag}$ ($H_0 = 70 \text{ km s}^{-1} \text{ Mpc}^{-1}$), diameters less than 1 kpc, and strong emission-lines superposed on a blue continuum. More recently, Gallego et al. (1996) spectroscopically classified as BCDs those galaxies showing intense, high-excitation emission lines and low $H\alpha$ luminosity ($L_{H\alpha} < 10^{41} \text{ erg s}^{-1}$; for $H_0 = 70 \text{ km s}^{-1} \text{ Mpc}^{-1}$). Finally, some variations on these definitions can be also found in the literature for selecting samples of BCD galaxies (Doublier et al. 1997; Kong & Cheng 2002).

In this paper we attempt to unify the concept of BCD by putting forward a new set of quantitative classification criteria. Using these criteria we are able to better include within the BCD class galaxies sharing common physical properties and evolutionary status and segregate them from other types of objects like dwarf irregulars (dIrr) and dwarf ellipticals (dE) or more massive star-forming galaxies. These criteria are sufficiently inclusive so as to also recover most of the galaxies traditionally classified as BCD.

Blue. Probably the most ill-defined property of the “Blue Compact Dwarf galaxies” is the color. Although the presence of a blue continuum in the optical spectra was already required by Thuan & Martin (1981) in their definition of BCDs, it was only a qualitative criterion. The observational criterion traditionally used has been the color of the highest surface brightness component since it was generally the only component detected in surveys using photographic plates. Thus, in order to establish a more quantitative criteria in this same sense we have determined the peak surface brightness (PSB) and the color at this peak surface-brightness from the surface-brightness profiles (Paper II) of the galaxies in our sample, both corrected for Galactic extinction. In order to reduce the effects of different seeing between the images we have averaged the color within the inner 3 arcsec of the profile; in those galaxies with optical diameter ≤ 20 arcsec we averaged the inner 1 arcsec.

Figure 1a shows the distribution in color at the PSB measured from the galaxies’ surface-

brightness. We have also plotted the colors at the PSB obtained for a sample of dIrr (Parodi, Barazza, & Binggeli 2002) and dE (Jerjen, Binggeli, & Freeman 2000) with published surface-brightness and $(B - R)$ color profiles. This figure shows a clear segregation between the color at the PSB of galaxies previously classified as BCDs and that of dIrr and dE, although an overlap is present. We have decided to impose a limit of $(B - R)$ color at the peak of $\mu_{B,\text{peak}} - \mu_{R,\text{peak}} \lesssim 1$. Using only this criterion many dE and most of the dIrr galaxies would be classified as BCDs. However, the combination with other criteria will improve the situation significantly (see below). Even with this wide limit some galaxies traditionally classified as BCD by other authors are apparently quite red. Particularly noticeable are the cases of UCM 0049–0045, UCM 1446+2312, and VCC 0001, that show peak color redder than $\mu_{B,\text{peak}} - \mu_{R,\text{peak}} = 1.2$ and should not be classified as BCDs.

Compact. With regard their compactness, Thuan & Martin (1981) set an upper limit to the optical diameter of BCDs of 1 kpc. However, observations carried out with CCDs during the 90’s have shown the presence of a very extended (up to a few kpc) low-surface-brightness component in many objects that were previously classified as BCDs. Therefore, the term “compact” in BCDs should be related more with the size of the high-surface-brightness component than with the total optical size. In other words, the compactness criterion should be more a surface brightness limit, like that used in Zwicky (1970), than a real physical-size limit.

In Figure 1b we show the distribution of peak surface brightness (PSB) measured from the galaxies B -band surface brightness profiles (to be presented in Paper II). This figure shows the PSB of BCDs being significantly brighter than that of dIrr (Parodi et al. 2002; Patterson & Thuan 1996) and dE (Jerjen et al. 2000). A fairly good separation between the different types is achieved imposing a limit of $\mu_{B,\text{peak}} < 22 \text{ mag/arcsec}^2$ to the PSB of BCDs. A total of 9 galaxies in our sample show PSB fainter than this value, so they should not be classified as BCDs. However, an individualized analysis of these objects shows that 6 of them are ≤ 20 arcsec in diameter that makes the atmospheric seeing significantly dim their PSB. Five of these objects (HS 0822+3542, UM 382, UM 417, SBS 0940+544C, NGC 4861) also show cometary morphology. Since the PSB have been determined from the azimuthally-averaged surface-brightness profiles, the PSB in these cases is measuring surface brightness at the peak of the low-surface-brightness component instead of the value at the burst located at the edge of the galaxy (Paper II). Finally, two of these objects should certainly not be classified as BCDs but as dIrr, II Zw33 B (Walter et al. 1997) and UGC 4483 (van Zee, Skillman, & Salzer 1998b).

The physical reason for the segregation observed in B -band PSB between the different galaxy types is the presence in the BCDs of a recent star formation event that outshines the

low-surface-brightness component. This event may be accompanied by blue optical colors and strong emission-lines (as in objects spectroscopically classified as HII galaxies). In dIrr and dE the recent star formation (if present) is comparatively less active and the PSB is consequently fainter and redder.

It is important to note that the fact that the segregation between BCDs and other types of dwarfs by PSB is better than the segregation by the color at the PSB is partially due to the different contribution of the red supergiants to the luminosity and color evolution of the burst (Doublier et al. 2001a).

Dwarf. One of the most important physical parameters driving the evolution of galaxies is the mass (see Brinchmann & Ellis 2000 and references therein). This is particularly important in the case of low-mass galaxies like the BCDs where it controls the formation of density waves or not. In this sense, the B -band luminosity cutoff imposed by Thuan & Martin (1981) was thought as a limit in the stellar mass of BCDs. However, the B -band luminosity is a very poor tracer of the stellar mass in a galaxy. Here we propose to use the K -band luminosity as a more reliable measure of the stellar mass in these galaxies (Gil de Paz et al. 2000a; Pérez-González et al. 2003a,b). In this regard it is worth mentioning that the assumption of different, plausible star formation histories within a galaxy may lead to changes in the mass-to-light ratio as high as a factor of 7 in the B -band but only a factor of 2 in K (Bell & de Jong 2001).

Unfortunately, the number of studies of BCDs in the near-infrared is still small and they are limited to a very few objects each (James 1994; Vanzi, Hunt, & Thuan 2002; Doublier, Caulet, & Comte 2001b; Noeske et al. 2003, submitted). In Figure 1c we have plotted the $(B - K)$ and $(B - R)$ colors for the 21 galaxies in our sample included in the 2MASS Second Incremental Release Extended Source Catalog (Jarrett et al. 2000). Dotted lines in this diagram represent the model predictions for a composite stellar population formed by a $Z_{\odot}/5$ metal-abundance burst with burst strength 1% (in mass) and age between 3.5 and 10 Myr. Thin, solid-lines correspond to the time evolution predicted by the models for the same burst with strength between 100% and 0.01%. The models used here are those developed by Gil de Paz et al. (2000a) and Perez-González et al. (2003a,b) which are based on the evolutionary synthesis models of Bruzual & Charlot (2003, unpublished). We have assumed that 15% of the Lyman continuum photons escape from the galaxy (or are absorbed by dust) before the ionization of the surrounding gas (see e.g. Gil de Paz et al. 2000a). This figure shows that there is a very good linear correlation between the integrated $(B - R)$ and $(B - K)$ color of these objects, which is also expected from the predictions of the models for burst strength values lower than 1% or $(B - R)$ colors redder than ~ 0.5 . The best fit to

this correlation is

$$(B - K) = 1.361 \times (B - R) + 1.63 \quad ; \quad \sigma = 0.25 \text{ mag} \quad (1)$$

As we commented above this relation is applicable only when the $(B - R)$ color is >0.5 mag. However, as we will show in Section 8 virtually all the BCD galaxies with $(B - R)$ color bluer than 0.5 mag have B -band absolute magnitude fainter than $M_B = -16.5$, so they can undoubtedly be classified as BCDs.

The average $(B - K)$ color of the 21 sample galaxies within 2MASS is 2.82 ± 0.42 . If we now apply this average $(B - K)$ color to the limit in B -band luminosity imposed by Thuan & Martin (1981) we end up with an equivalent limit in K -band luminosity of $M_K > -21$ mag (for $H_0 = 70 \text{ km s}^{-1} \text{ Mpc}^{-1}$). In Figure 1d we show the frequency histogram of K -band absolute magnitudes of the galaxies in our sample obtained applying the Equation 1. Noteworthy, from the 9 galaxies in our sample showing $M_B < -18.15$ mag only 5 are brighter than $M_K = -21$ mag. Within them IC 10 is probably above this limit because of its uncertain galactic extinction correction. The other 4 galaxies should not be classified as BCD galaxies, II Zw 33, Mrk 7, Tol 1924–416, and Mrk 314. The galaxies showing $M_B < -18.15$ mag but $M_K > -21$ mag (KUG 0207–016A, Mrk 400, Haro 2, Pox 4) are probably relatively low-mass objects experiencing a very massive burst that makes their integrated colors bluer than the average. Individualized near-infrared observations are necessary to confirm this.

Summarizing, we propose that, in order to be classified as a BCD, a galaxy has to fulfill the following observational, quantitative criteria: (1) it has to be *blue*, $\mu_{B,\text{peak}} - \mu_{R,\text{peak}} \lesssim 1$, (2) *compact*, $\mu_{B,\text{peak}} < 22 \text{ mag/arcsec}^2$, and (3) *dwarf*, $M_K > -21$ mag. As we have shown above these criteria recover most of the galaxies traditionally classified as BCDs and also allow to segregate the BCDs from other types of dwarf galaxies like dIrr or dE.

4. Observations

We have observed the whole sample of 114 galaxies in B , R , and in the light of $H\alpha$ during a total of 11 observing runs between June 2001 and July 2002. Nine of the observing runs were carried out at the Palomar Observatory 60-inch telescope using CCD Camera with the 2048×2048 pixel CCD#13 attached. The pixel scale was 0.378 arcsec/pixel. Two additional observing runs were carried out at the du Pont 100-inch telescope in Las Campanas Observatory (Chile) between February 8-9 2002 and March 5-9 2002. We used the Direct CCD with the 2048×2048 pixel Tek5 CCD attached, which, placed at the Cassegrain focus of the telescope, gives a scale of 0.260 arcsec/pixel. In Table 2 we give a summary of the

observing runs and the properties of the detectors used (gain, readout noise, etc).

Typical exposure times in B , R , and $H\alpha$ were, respectively, 15, 45, and 90 min at Palomar Observatory and 15, 15, and 30 min at Las Campanas. A total of 86 galaxies were observed at Palomar Observatory and 28 at Las Campanas. The seeing (FWHM) in the images ranged from 0.6 arcsec (Tol 002 in R) to 4.3 arcsec (Haro 14 in B). The median seeing values in B , R , and $H\alpha$ were 1.8, 1.6, and 1.5 arcsec, with 80 per cent of the galaxies having seeing better than 2.5, 2.0, and 1.9 arcsec, respectively. The image quality at Las Campanas Observatory was significantly better than at Palomar Observatory. In this sense, the median seeing of the B , R , and $H\alpha$ images taken at Las Campanas were 1.1, 0.9, and 0.9 arcsec, respectively, whereas at Palomar Observatory the median seeing values achieved were 2.0, 1.7, and 1.6 arcsec. In Table 3 we give a summary of the characteristics of some of the images contained in this Atlas, including observatory, telescope, date, exposure time, number of frames, airmass, and FWHM (the complete table is available in the electronic version of the paper). The date of observation given in this table corresponds to the civil date at the start of the observing night.

In Figure 2 we give the spectral response functions of the filters used in this Atlas as provided by the manufacturers. Thin continuous-lines correspond to the filters used at the Palomar Observatory 60-inch telescope and broad-lines to those used at Las Campanas 100-inch telescope. This figure clearly shows that the Johnson- B and Cousins- R filters used in this Atlas are very similar to those used by Landolt (1992a) to build his list of standard stars (dotted-line) and also similar to those originally used to define the Johnson-Cousins system (dashed-line; B -band: Azusienis & Straizys 1969; R -band: Bessell 1990). It is worth noting that our filters as plotted have been convolved with the spectral response functions of the corresponding detectors. This could be, in part, the reason for the apparently-poorer spectral response of our filters to wavelengths longer than ~ 6500 Å compared to those used by Landolt (1992a) and Bessell (1990). Narrow-band filters used at Palomar and Las Campanas were 20 Å and 65 Å wide, respectively. The use of narrower $H\alpha$ filters at Palomar Observatory reduced the contribution of the continuum to the photon noise of the $H\alpha$ images, partially compensating for both the poorer image quality of the $H\alpha$ images obtained at Palomar Observatory and the smaller collecting area of the 60-inch telescope.

5. Reduction

The images were reduced following the standard procedures of bias subtraction and flat-fielding using the IRAF⁴ task CCDPROC. The dark current in both detectors used was negligible (≤ 1 count/hour/pixel) and no dark subtraction was applied. In those cases where three or more frames in one band were obtained for the same object the cosmic rays were rejected using the IRAF task IMCOMBINE. When only one or two images were available we removed the cosmic rays interactively using the IRAF tasks COSMICRAYS and CREDIT within the CRUTIL package.

5.1. Flux-calibration

Considering the relatively small number of nights that were photometric (12 out of 49) we decided to use the following strategy in order to flux-calibrate our images. During the non-photometric nights at Palomar and Las Campanas observatories we obtained very deep exposures in R and $H\alpha$. During the photometric nights the adopted follow-up strategy was slightly different at each site. At Palomar we took short (600-900 s) B and R exposures of the same objects already observed in R and $H\alpha$, along with images of a large number of photometric standards (Landolt 1992a). Then, using the fluxes of the field stars in the calibrated R -band, deep R and $H\alpha$ images along with the filter+detector response functions (see Figure 2) we cross-calibrated our deep R and $H\alpha$ images (see Appendix A). At Las Campanas, during the photometric nights we observed both objects and spectrophotometric standards (Hamuy et al. 1992; Landolt 1992b) through all B , R and $H\alpha$ filters. During these nights we also took short B and R exposures of the objects already observed in R and $H\alpha$ during previous non-photometric nights. The flux calibration of the $H\alpha$ images taken during non-photometric conditions was carried out in the same manner as the Palomar case (see Appendix A). The coefficients obtained from the calibration are given in Table 4. This strategy has allowed us to make optimal use of telescope time, achieving relatively small photometric errors (see Table 5). In order to check the reliability of the $H\alpha$ calibration based on the use of R -band calibrated data, we compared the results obtained from this method with those resulting from the observation of spectrophotometry standards through the $H\alpha$ filters during the Las Campanas photometric nights. The calibration results agreed to within 5%.

⁴IRAF is distributed by the National Optical Astronomy Observatories, which are operated by the Association of Universities for Research in Astronomy, Inc., under cooperative agreement with the National Science Foundation.

The continuum-subtracted H α images of our sample were obtained from the R -band and line+continuum H α images making use of the equations given in Appendix A. Briefly, we compared the flux in counts of a large number of field stars (>30) both in the R -band and H α images. Then, using the IRAF task GAUSS the image with the best seeing was convolved with a gaussian kernel to match the seeing of the worst-quality image. Finally, we divided the R -band image by the corresponding scaling factor and subtracted it from the line+continuum H α image. Residuals in the continuum-subtracted images due to the presence of very bright field stars were removed interactively using the IRAF task CREDIT within the CRUTIL package. For more details about this procedure and the flux-calibration of the resulting continuum-subtracted H α image the reader is referred to Appendix A.

5.2. Astrometry

In order to perform the astrometry on the images we first aligned all the frames in the same band taken on the same night for the same object using the IRAF task IMSHIFT and the positions of a few field stars. Then, using the positions of a larger number of field stars (>100), as given by the IRAF task STARFIND, we registered the images in the different bands using the GEOMAP and GEOTRAN tasks. Finally, once all the frames were combined and the various bands registered, we used the IRAF tasks STARFIND and CCXYMATCH to cross-correlate the positions of the field stars in pixels with their FK5 equatorial coordinates in the USNO-A2.0 catalogue. The cross-correlation was done using the positions of the stars in our final R -band image. The H α (line+continuum) image was used in those cases where a large number of USNO-A2.0 stars were saturated in the R -band image (e.g. in those cases of exceptional seeing). Once the plate solution was computed and stored in the image header (using the IRAF tasks CCMAP and CCSETWCS) we copied the WCS information to the rest of the bands using the task WCSCOPY. Typical (rms) errors in the astrometric calibration of our images are 0.1 arcsec both in RA and DEC.

6. Maps and Morphological Classification

In Figure 3 we present greyscale maps corresponding to the R -band and to continuum-subtracted H α images obtained for the 114 galaxies in our sample. A blow-up of the nuclear region is also shown in the upper right-hand corner of each image, rescaled in intensity to emphasize details. The size of the compass shown in each of the images is 0.5 kpc at the distance of the corresponding galaxy. The average limiting surface brightness of the main images (3σ) are $24.6 \text{ mag arcsec}^{-2}$, $24.3 \text{ mag arcsec}^{-2}$, and $7 \times 10^{-17} \text{ erg s}^{-1} \text{ cm}^{-2} \text{ arcsec}^{-2}$ for

B , R , and $H\alpha$, respectively.

Within the galaxy sample studied only three galaxies were not detected by us in $H\alpha$ emission, namely Mrk 709, UCM 1446+2312, and UGC 4703 NOTES02. In the case of Mrk 709 the galaxy recession velocity provided by NED ($1,197 \text{ km s}^{-1}$), which was taken from the 21cm-line velocity data published by van Zee, Haynes, & Giovanelli (1995), differs significantly from that published by Terlevich et al. (1991) ($\sim 15,000 \text{ km s}^{-1}$) and recently confirmed by E. Pérez-Montero (private communication). This leads us to suggest that the low-redshift HI emission detected by van Zee et al. (1995) is not related to Mrk 709, but maybe with another object in the beam that, according to our data, does not show significant ionized gas emission. For UCM 1446+2312 the uncertainty in the recession velocity (determined from the position of the $H\alpha$ line in objective-prism photographic plates; Alonso et al. 1999) is $\sim \pm 1,200 \text{ km s}^{-1}$. Therefore, the line-emission arising from this object might well be beyond the wavelength region covered by the 20 \AA -wide filter used. Finally, UGC 4703 NOTES02 forms with UGC 4703 NOTES01 an interacting pair where only the latter shows $H\alpha$ emission. This suggests that UGC 4703 NOTES02 may have either exhausted most of its gas early during its evolution, or it may have lost it as consequence of the interaction with UGC 4703 NOTES01. Is it important to note that, as already pointed out by Cairós et al. (2001a) and we have discussed in Section 3, most of the BCD galaxies were originally identified by their high surface brightness and blue optical colors. Therefore, some of them may be expected to show very low $H\alpha$ equivalent widths (EW) (i.e. they are BCDs but they should not be then classified as HII galaxies). Some examples of this may be Mrk 1423 and I Zw 115 (see Section 8).

The maps presented in Figure 3 show that most of the galaxies in our sample have an extended, low-surface-brightness halo visible in the continuum images. Such halos, commonly associated with an evolved stellar population (Papaderos et al. 1996; Cairós et al. 2001a,b and references therein), are usually more extended than the region showing $H\alpha$ emission, except perhaps in the case of the most compact objects (I Zw 18, HS 0822+3542, Pox 186). In Paper II we analyze the structural properties of this low-surface brightness component. With regard to the morphology in $H\alpha$ the inspection of our images show that 83 galaxies in our sample (73%) show star formation activity distributed over more than one region. In particular, in 45 galaxies (39%) we are able to distinguish 4 regions or more. Only 28 galaxies show their morphology in the light of $H\alpha$ to be dominated by only a single, nuclear HII region. It is worth noting that the median distance and seeing for those galaxies showing only one single star-forming region are 23 Mpc and 1.4 arcsec respectively, while the galaxies with multiple regions are typically at 19 Mpc and have 1.5 arcsec seeing. Clearly, the difference between these values is not large enough to explain the different number of regions detected purely in terms of a differing spatial resolution.

Based only on broad-band optical imaging data, Loose & Thuan (1986) undertook a morphological classification of BCD galaxies. They defined four different groups:

- **iE BCDs.** These are galaxies with an outer diffuse halo with elliptical isophotes and inner irregular isophotes due to the presence of multiple star-forming regions and star clusters.
- **nE BCDs.** These objects show an elliptical halo and a clearly defined nucleus.
- **iI BCDs.** These galaxies have an irregular outer halo and an off-center nucleus. Within this class Loose & Thuan (1986) also defined
 - iI,C BCDs** – Cometary morphology.
 - iI,M BCDs** – Apparent mergers.
- **i0 BCDs.** These are galaxies not showing a diffuse extended component in the broad-band images.

The classification of a galaxy as nE or iE BCD is been mainly determined by the shape of the inner isophotes: regular in the case of nE, and irregular for the iE BCDs. However, the greyscale maps presented in Figure 3 show that, in some cases, despite the continuum isophotes in the inner region being regular, the $H\alpha$ images may show a complex structure composed of several individual HII regions. An example of this behavior is seen in Mrk 409, where the inner R -band isophotes are regular (which would lead one to classify this galaxy as a nE BCD), but the $H\alpha$ emission shows the presence of a ring composed of at least 5 HII regions (see Figure 3). In cases like that of Mrk 409 we have made use of the information provided by the $H\alpha$ images, and the galaxies have been reclassified as iE BCDs. The presence of a ring of star-forming regions around the nucleus of the galaxy has been observed in a total of 4 objects in our sample including Mrk 409, namely Mrk 86 (see Gil de Paz et al. 2000b,c; 2002), Mrk 400, Mrk 409, and VCC 0655. The radius of this ring ranges from 0.5 to 1.0 kpc. In these cases we have added a letter ‘r’ to the morphological type of the objects.

The results of the morphological classification are given in Table 5. For the objects with detected $H\alpha$ emission 27 out of 111 (24%) were classified as nE BCDs, 37 (33%) as iE, and 39 (35%) as iI. For the 39 iI BCDs, 11 are “cometary” (iI,C) and 10 are “mergers” (iI,M). In only 8 galaxies did we not detect any underlying/extended R -band continuum light (that would be otherwise be associated with an old stellar population) and, consequently, they were classified as i0 BCDs. Within this group are the objects with the lowest metallicity in our sample (I Zw 18, Tol 65, UCM 1612+1308). For comparison, within their sample of 28

BCDs, Cairós et al. (2001a,b) found 21% of nE, 39% of iE, and 32% of iI BCDs (7% and 14% of the total were iI,C and iI,M BCDs, respectively).

It is worth mentioning that, although the fraction of BCDs with elliptical envelopes is <60 per cent, the four galaxies where a ring of star-forming regions was found are all iE BCDs. This fact suggests that the shaping of these rings requires a highly symmetric distribution of the galaxy stellar and total mass.

7. FITS Images

The FITS copies of the images in this Atlas are publicly available individually through the NED image server at <http://nedwww.ipac.caltech.edu/forms/images.html> and as a collection through a dedicated web page at http://nedwww.ipac.caltech.edu/level5/Sept02/Palco_BCD/frames.html. The FITS headers of these images include, in a homogeneous and self-explanatory way, all the information regarding the image WCS solution and flux calibration along with the date of observation, telescope, filter, exposure time, etc (see also Table 3). A CDROM with the complete set of FITS images may also be requested from the first author.

8. Integrated Photometry

In order to obtain integrated photometry of the galaxies in our sample we edited the final, flux-calibrated images of the Atlas. Field stars and background galaxies falling near the position of our galaxies were removed using the IRAF task CREDIT within the CRUTIL package. We did this for all the *B* and *R*-band images. Emission from field stars and from background galaxies in the $H\alpha$ images was removed at the time of the $H\alpha$ continuum subtraction.

The criteria for identifying a region as belonging to the galaxy (or not) were those used by Gil de Paz et al. (2000b). Briefly, these criteria are based (1) on the size and ellipticity of the emitting region compared to the image PSF, (2) the presence of $H\alpha$ emission associated with the region, and (3) the distance of the region from the galaxy center (see Gil de Paz et al. 2000b for more details).

Once all the images were edited we defined two sets of polygonal apertures. The first set was constructed to include the total integrated light originating from the galaxy at continuum wavelengths, and it was identically used to measure both the *B* and *R*-band integrated magnitudes. Due to the different spatial distribution and morphology of the

H α emission compared with the continuum, the integrated H α fluxes were measured using different sets of polygonal apertures. In both cases, the integrated fluxes were obtained using the IRAF task POLYPHOT.

The color term required to determine the B and R -band magnitudes of the galaxies was first computed assuming a mean $(B - R)$ color of 0.8 mag and using the color coefficients given in Table 4. However, the integrated colors derived were in some cases significantly different from this average value. The final magnitudes and colors were then iteratively computed using the limit of the following sequence as the best $(B - R)$ color for the galaxy,

$$(B - R)_{i+1} = (B - R)_i + (k_{B,B-R} - k_{R,B-R}) \times ((B - R)_i - (B - R)_{i-1}) \quad (2)$$

where $k_{B,B-R}$ and $k_{R,B-R}$ are the color coefficients for the B and R bands, respectively. This sequence ranges from $i=1$ to n , where $(B - R)_0=0.8$ mag and $(B - R)_1$ is the integrated color initially measured on the images. Convergence ($\Delta(B - R) \ll 0.01$) occurred after a few ($n \sim 5-10$) iterations. The final magnitudes and colors are given in Table 5. The errors shown in this table were obtained by combining the photometry errors given by the task POLYPHOT with those associated with the calibration of the images. Fluxes, magnitudes and colors shown are corrected for Galactic extinction (using the values given in Table 1 and the Galactic extinction law of Cardelli, Clayton, & Mathis 1989), but they are not corrected for internal extinction. H α fluxes given in Table 5 are also corrected for underlying stellar absorption adopting an equivalent width of -3 \AA (González-Delgado, Leitherer, & Heckman 1999).

We have compared our integrated magnitudes measured with the asymptotic values given by Doublier et al. (1997, 1999) and Cairós et al. (2001b) and the B_T and R_T magnitudes in the RC3 and ESO-LV catalogs (B_T , de Vaucouleurs et al. 1991; B_T , R_T ; Lauberts & Valentijn 1989). The mean difference between the B -band magnitudes given by Cairós et al. (2001b) and ours for a total of 14 galaxies in common is +0.06 mag with an rms of ± 0.22 mag (our magnitudes are marginally brighter). The comparison between the total B -band magnitudes in the RC3 catalogue and our observed magnitudes gave a difference of -0.04 ± 0.19 mag (44 galaxies in common). The largest B -band difference ($+0.36 \pm 0.34$ mag) is obtained when comparing with the results for 23 galaxies in common with Doublier et al. (1997, 1999). For the R -band data the differences are -0.22 ± 0.20 mag (11 galaxies) and -0.15 ± 0.36 mag (26 galaxies) with respect to the Cairós et al. (2001b) and Doublier et al. (1997, 1999) samples, respectively. This systematic difference is reduced to -0.05 ± 0.16 mag (9 galaxies) when comparison is made with the R -band magnitudes in the ESO-LV catalogue. Note that the comparison with the RC3 and ESO-LV catalogs was done using observed magnitudes (i.e. not corrected for Galactic extinction). Finally, we compared the aperture-photometry data of Cairós et al. (2001a) with our results. This yields differences of $+0.16 \pm 0.18$ mag (14 galax-

ies) and -0.10 ± 0.23 mag (11 galaxies) in the B and R bands, respectively. The existence of these differences is attributed to (1) intrinsic differences between the extrapolated asymptotic magnitudes and our aperture-photometry data, (2) the different galactic-extinction maps used (Burstein & Heiles 1984 or Schelegel et al. 1998), and (3) the different methods adopted for the removal of field stars and background galaxies falling near the position of the galaxies under study.

Absolute magnitudes and $H\alpha$ luminosities were derived using the distances given in Table 1. We computed the equivalent widths of $H\alpha$ by dividing the $H\alpha$ flux by the flux (per unit wavelength) in the R -band after taking into account the added contribution of $H\alpha$ to the observed R -band magnitude itself (see Appendix A for more details).

In Figures 4a & 4b we show the frequency histograms in $(B - R)$ color and B -band absolute magnitude. Average color and absolute magnitude of the galaxies in our sample are $(B - R) = 0.7 \pm 0.3$ mag and $M_B = -16.1 \pm 1.4$ mag. The average $H\alpha$ luminosity is $\log(L_{H\alpha}) = 40.0 \pm 0.6$ (erg s^{-1}). In Panels 4c, 4d, 4e, and 4f we have plotted, respectively, $(B - R)$ vs. M_B , $\text{EW}(H\alpha)$ vs. M_B , $L_{H\alpha}$ vs. M_B , and $\text{EW}(H\alpha)$ vs. $(B - R)$, using different symbols for each morphological type (dots, nE; filled-stars, iE; open-squares, iI; open-circles, i0).

Figure 4c shows that fainter BCD galaxies tend to have bluer colors. Also the galaxies classified as iI and i0 BCD show, on average, bluer colors than those in the nE and iE classes. This same difference is also present in the case of the $\text{EW}(H\alpha)$ (see Figure 4d), where iI and i0 BCDs show significantly larger equivalent widths. The average colors and equivalent widths of the nE and iE BCDs are $(B - V) = 0.8$ mag and $\text{EW}(H\alpha) = 90 \text{ \AA}$, respectively, while for the iI and i0 BCDs these values are $(B - V) = 0.5$ mag and $\text{EW}(H\alpha) = 200 \text{ \AA}$. If we consider only the galaxies classified as iI BCDs the average colors and $\text{EW}(H\alpha)$ values derived are 0.6 mag and 150 \AA , respectively. Moreover, Figure 4c also shows that for $(B - R) < 0.5$ about 27% (6 over 22) of the galaxies are nE/iE types while for $(B - R) > 0.95$ this percentage goes up to 95% (18/19). With regard to the equivalent width of $H\alpha$, Figure 4d indicates that for $\log \text{EW}(H\alpha) > 2.4$ about 23% (3/13) are nE/iE BCDs while for $\log \text{EW}(H\alpha) < 1.2$ the percentage is 100% (14/14). The lack of objects showing both low continuum and $H\alpha$ luminosity (lower-right corner of Figure 4d) is mainly due to the selection effects associated with the objective-prism surveys searching for emission-line galaxies from whose many galaxies in our sample were selected. In these surveys the probability of detection is mainly driven by the emission-line flux and its contrast against the continuum (Salzer 1989). Therefore, objects with low luminosity will be detected only if the contrast between the line and the continuum is very strong, in other words, if the equivalent width is large ($> 20 \text{ \AA}$ typically).

The dotted-line in Figure 4e represents the model predictions for a composite stellar

population formed by a 3.5-Myr-old burst with $Z_{\odot}/5$ metallicity and 1% burst strength in mass superimposed on a 9-Gyr-old underlying stellar population with the same metallicity. The independent effects of a change in the age of the burst, the internal extinction and total mass of the galaxy are also shown. These models were extensively described in Section 3.

Finally, in Figure 4f we show the distribution of our galaxies in the $\text{EW}(\text{H}\alpha)$ vs. $(B - R)$ color diagram along with the predictions of the same models for different values of the burst age and burst strength, ranging from 3.5 to 10 Myr and from 0.01 to 100%, respectively. This figure shows that in most of the BCDs in our sample ($\sim 80\%$) the presence of an evolved, underlying stellar population is required, even if a moderate internal extinction of $E(B - V) = 0.2$ mag is assumed and differences in metallicity between individual galaxies are taken into account. This value of the color excess corresponds to the most frequently found value in the spectroscopic atlas of BCDs of Terlevich et al. (1991). The most metal-poor objects in our sample, however, do not appear to require an evolved stellar population to reproduce their $(B - R)$ colors and $\text{EW}(\text{H}\alpha)$. But, the $(B - R)$ color is not very sensitive to the presence of an evolved stellar population when the burst strength is larger than a few percent, so the existence in these galaxies of such an evolved population cannot be ruled out by these data. The combination of optical data and deep near-infrared observations is crucial in solving this problem (James 1994; Doublier et al. 2001b, Vanzi et al. 2002; Noeske et al. 2003, submitted).

Figure 4f also confirms (see above) that there is a clear difference between the properties of the nE/iE BCDs (filled symbols) and those of the iI/iO BCDs (open symbols). BCD galaxies classified as nE and iE types are significantly redder and show lower EWs in $\text{H}\alpha$ than the iI and iO BCDs. This is probably due to (1) a lower dust extinction, (2) higher burst strength, and/or (3) lower metallicity of the iI and iO galaxies compared to the nE and iE BCDs. Some differences in this same sense have been already pointed out by Noeske et al. (2000) for the case of the iI,C (cometary) BCDs.

It is worth noting that, despite the number of surveys involved, different selection criteria, and different physical sizes and environments where these galaxies were discovered, there are observational properties that are common to all BCD galaxies within the same morphological class, although with a significant dispersion. This suggests that the morphology of these galaxies is direct testimony to their merging and star-formation histories.

In order to show the wide range of morphologies and physical sizes spanned by these galaxies, and its relation to their luminosities and optical colors, we have plotted together the R -band and $\text{H}\alpha$ maps for 80 of the galaxies in the sample set to a common distance and using a common surface brightness scale (see Figures 5 and 6). Due to the dense clustering of galaxies at certain positions in the color-magnitude diagram (see Figure 4c)

the representation of the complete sample of 114 objects in Figures 5 and 6 is not possible. The R -band and $H\alpha$ images of the galaxies are shown in boxes of fixed physical size of 5 kpc on a side using a gray scale ranging from the sky level (white) to a surface brightness of 21 mag/arcsec⁻² in R and 1.5×10^{-15} erg s⁻¹ cm⁻² arcsec⁻² in $H\alpha$ (black) (these surface brightness are observed values, except for the highly obscured objects II Zw 40 and IC 10 which were corrected for Galactic extinction). Figure 6 shows that, as commented on above, the largest $H\alpha$ EWs are found within those objects showing the lowest luminosities and bluest colors (bottom-right in this figure). These images also graphically illustrate that BCD galaxies cover, at least, one order of magnitude in physical size, from ~ 0.3 kpc to ≥ 3 kpc. A more detailed analysis of the physical size, structure, and population content of BCDs will be carried out in subsequent papers.

9. Conclusions

Summarizing,

- B , R , and $H\alpha$ images for a total of 114 galaxies have been obtained. According to the new set of criteria proposed to define the Blue Compact Dwarf class of galaxies all except 9 objects (II Zw 33, Mrk 7, Tol 1924–416, Mrk 314, II Zw 33B, UGC 4483, UCM 0049–0045, UCM 1446+2312, & VCC 0001) are classified as BCDs. This represents an increase of a factor of ~ 4 with respect to similar previous studies (Doublrier et al. 1997, 1999; Cairós et al. 2001a,b). Indeed, previous studies were mostly based on only broad-band imaging data.
- The new set of criteria proposed for defining a galaxy as a BCD includes a limit in K -band luminosity ($M_K > -21$ mag), the peak surface brightness ($\mu_{B,\text{peak}} < 22$ mag/arcsec²), and the color at the peak surface brightness ($\mu_{B,\text{peak}} - \mu_{R,\text{peak}} \lesssim 1$).
- The flux-calibrated and WCS-compliant images of the Atlas are publicly available through the NASA/IPAC Extragalactic Database (NED) image service on a object-by-objects basis and through a dedicated web page within LEVEL5: A Knowledgebase for Extragalactic Astronomy & Cosmology (<http://nedwww.ipac.caltech.edu/level5/>).
- In all but three galaxies we detect $H\alpha$ -line emission. About 73% of the galaxies show $H\alpha$ emission distributed in more than one region (39% in 4 or more regions). Morphologically, 24% of the galaxies are classified as nE BCDs, 33% as iE, 35% as iI (10% cometary BCDs -iI,C- and 9% mergers -iI,M-), and 7% as i0 BCDs (see Loose & Thuan 1986). Four of the galaxies (Mrk 86, Mrk 400, Mrk 409, VCC 0655) show a nuclear ring of star-forming regions with radius 0.5-1 kpc.

- Average colors, absolute magnitudes and $H\alpha$ luminosities of the sample are $(B - R) = 0.7 \pm 0.3$ mag, $M_B = -16.1 \pm 1.4$ mag, and $\log(L_{H\alpha}) = 40.0 \pm 0.6$ (erg s^{-1}). Galaxies classified as nE and iE BCDs show, on average, redder colors and lower $H\alpha$ equivalent widths than those classified as iI and iO BCDs. This is also true if only the iI-type BCDs are considered.
- For most of the galaxies ($\sim 80\%$) the integrated $(B - R)$ colors and $H\alpha$ equivalent widths require the presence of an evolved, underlying stellar population in addition to a young population with burst strength lower than 10% in mass. The most metal-poor BCDs (I Zw 18, Tol 65, UCM 1612+1308) are found in that 20% of the sample whose properties are compatible with the evolution of a pure, young burst. They also show the bluest colors and highest equivalent widths within the sample. However, due to the degraded sensitivity of the $(B - R)$ color to the presence of an underlying stellar population for burst strengths $\geq 10\%$, the use of deep near-infrared imaging data will be required to further investigate, in a statistical way, their nature as young galaxies.

We are grateful to the Palomar and Las Campanas observatories staff for their support and hospitality, and to the Caltech/Palomar and OCIW/Las Campanas Time Allocation Committees for the generous allocation of time to this project. AGdP acknowledges financial support from NASA through a Long Term Space Astrophysics grant to BFM. AGdP is also partially supported by the CONACYT (Mexico) grant 36132-E and the Spanish Programa Nacional de Astronomía y Astrofísica under grant AYA2000-1790. This research has made use of the NASA/IPAC Extragalactic Database (NED) which is operated by the Jet Propulsion Laboratory, California Institute of Technology, under contract with the National Aeronautics and Space Administration. We would like also to thank K. G. Noeske, P. G. Pérez-González, and C. Sánchez Contreras for valuable discussions and the NED/LEVEL5 staff for helping us making this Atlas publicly available. For technical support on using the images from this atlas, please write to ned@ipac.caltech.edu or to one of the authors (agpaz, barry, olga@ipac.caltech.edu). We are grateful to the anonymous referee for her/his helpful comments and suggestions.

A. Emission-line continuum subtraction using broad-band images

Some of the expressions derived in this appendix also appear in Waller (1990). Here we have carried out a more detailed analysis of the procedures used for flux-calibrating broad- or narrow-band imaging data. We have also considered the case that the field stars used for the normalization of the continuum image have absorption features in their spectra and considered the presence of other emission-lines in the galaxy spectrum (e.g. the [NII] $\lambda\lambda 6548, 6584$ ÅÅ doublet in our H α filters) within the narrow-band filter used.

We consider two images, one taken with a narrow-band filter (≤ 100 Å; NB hereafter) and another taken with a broad-band one (≥ 1000 Å; BB hereafter). If we would be observing an astronomical object having a line in emission within the wavelength range of these filters, the total fluxes obtained (in counts after the sky subtraction) would be

$$f_{\text{NB}} = g_{\text{NB}} \times \left(\int f_{\text{cont},\lambda} S_{\text{NB},\lambda} d\lambda + \int f_{\text{line},\lambda} S_{\text{NB},\lambda} d\lambda \right) \quad (\text{A1})$$

$$f_{\text{BB}} = g_{\text{BB}} \times \left(\int f_{\text{cont},\lambda} S_{\text{BB},\lambda} d\lambda + \int f_{\text{line},\lambda} S_{\text{BB},\lambda} d\lambda \right), \quad (\text{A2})$$

respectively for the NB and BB filters, where g_{NB} and g_{BB} are the ratios between counts and flux in $\text{erg s}^{-1} \text{cm}^{-2}$ (including exposure time, gain, system total efficiency, and atmospheric extinction), $f_{\text{line},\lambda}$ and $f_{\text{cont},\lambda}$ are the fluxes per unit wavelength (in units of $\text{erg s}^{-1} \text{cm}^{-2} \text{Å}^{-1}$) emitted by the object due to the line and the continuum, respectively, and $S_{\text{line},\lambda}$ and $S_{\text{cont},\lambda}$ are the normalized response functions of the NB and BB (including both the filter and detector efficiency), respectively.

Assuming that the continuum is approximately flat in the spectral region of both filters, we can write

$$f_{\text{NB}} \simeq g_{\text{NB}} \times \left(\text{FWHM}_{\text{NB}} f_{\text{cont},\lambda} + \int f_{\text{line},\lambda} S_{\text{NB},\lambda} d\lambda \right) \quad (\text{A3})$$

$$f_{\text{BB}} \simeq g_{\text{BB}} \times \left(\text{FWHM}_{\text{BB}} f_{\text{cont},\lambda} + \int f_{\text{line},\lambda} S_{\text{BB},\lambda} d\lambda \right) \quad (\text{A4})$$

where FWHM is the Full Width at Half Maximum of the corresponding filter.

If we now consider that the width of the emission-line is significantly narrower than the NB filter (less than $1/10^{\text{th}}$ the FWHM_{NB}) we can simplify these expressions to

$$f_{\text{NB}} \simeq g_{\text{NB}} \times (\text{FWHM}_{\text{NB}} f_{\text{cont},\lambda} + f_{\text{line}} S_{\text{NB, line}}) \quad (\text{A5})$$

$$f_{\text{BB}} \simeq g_{\text{BB}} \times (\text{FWHM}_{\text{BB}} f_{\text{cont},\lambda} + f_{\text{line}} S_{\text{BB, line}}), \quad (\text{A6})$$

where f_{line} is the total flux of the emission line (in $\text{erg s}^{-1} \text{cm}^{-2}$) and $S_{\text{NB, line}}$ and $S_{\text{BB, line}}$ are the normalized responses of the filters at the wavelength of the emission line.

Then, defining

$$\beta = \frac{\text{FWHM}_{\text{NB}}}{\text{FWHM}_{\text{BB}}} \quad (\text{A7})$$

$$\gamma = \frac{g_{\text{NB}}}{g_{\text{BB}}} \quad (\text{A8})$$

$$\delta = \frac{S_{\text{NB,line}}}{\beta} - S_{\text{BB,line}} \quad (\text{A9})$$

$$\epsilon = \frac{S_{\text{BB,line}}}{S_{\text{NB,line}}} \quad (\text{A10})$$

we obtain f_{line} , $f_{\text{cont},\lambda}$, and the equivalent width of the line (EW) as

$$f_{\text{line}} = \frac{1}{g_{\text{NB}} \beta \delta} (f_{\text{NB}} - \beta \gamma f_{\text{BB}}) = \frac{1}{g_{\text{BB}} \beta \gamma \delta} (f_{\text{NB}} - \beta \gamma f_{\text{BB}}) \quad (\text{A11})$$

$$f_{\text{cont},\lambda} = \frac{\gamma}{g_{\text{NB}} \text{FWHM}_{\text{NB}} \left(\frac{1}{\beta} - \epsilon\right)} \left(f_{\text{BB}} - \frac{\epsilon}{\gamma} f_{\text{NB}}\right) = \frac{1}{g_{\text{BB}} \text{FWHM}_{\text{BB}} (1 - \epsilon \beta)} \left(f_{\text{BB}} - \frac{\epsilon}{\gamma} f_{\text{NB}}\right) \quad (\text{A12})$$

$$\text{EW}_{\text{line}} = \text{FWHM}_{\text{BB}} \frac{(1 - \epsilon \beta)}{\beta \gamma \delta} \frac{(f_{\text{NB}} - \beta \gamma f_{\text{BB}})}{\left(f_{\text{BB}} - \frac{\epsilon}{\gamma} f_{\text{NB}}\right)} \quad (\text{A13})$$

In order to solve these equations (and obtain the pure emission-line image of the object) we need to determine the β , γ , δ , and ϵ parameters. The β , δ , and ϵ parameters can be easily obtained from the normalized response function of the NB and BB filters given the rest-frame wavelength of the emission-line considered and the recession velocity of the object.

With regard to the γ parameter two approaches can be followed. First, we can determine the value of the γ parameter if both the NB and BB images are flux-calibrated just dividing the corresponding calibration factors. However, this parameter can be also measured without flux-calibrating any of the two images. In this sense, we can measure the total counts on both images for a large number of objects with well-known spectral properties in the wavelength range of interest. In the case of the line equivalent width, it is not necessary either to calibrate any of the images since Equation A13 does not depend on g_{NB} or g_{BB} . On the other hand, if we are interested in deriving the emission-line flux (or the continuum flux) of the object at least one of the images should be flux-calibrated.

Thus, with regard to the derivation of γ , if we measure the total counts on both the NB and BB for a number of *featureless* objects (usually field stars) we get

$$f_{\text{NB}} = g_{\text{NB}} \times \text{FWHM}_{\text{NB}} f_{\text{cont},\lambda} \quad (\text{A14})$$

$$f_{\text{BB}} = g_{\text{BB}} \times \text{FWHM}_{\text{BB}} f_{\text{cont},\lambda}, \quad (\text{A15})$$

which leads to

$$\gamma = \frac{1}{\beta} \frac{f_{\text{NB}}}{f_{\text{BB}}} \quad (\text{A16})$$

This is the most commonly used method for subtracting the continuum contribution in narrow-band images. This method is particularly simple and powerful because the $f_{\text{NB}}/f_{\text{BB}}$ ratio ($=\beta \times \gamma$) can be used to scale the BB image to the NB one and obtain a pure emission-line image without any previous knowledge about the filters response functions.

In addition, in some cases it is not possible to find *featureless* stars usually because the emission-line of interest (or other lines) are present in absorption (or emission) in their spectra. In that case the Equation A16 has to be substituted by

$$\gamma = \frac{1 + \sum_i \frac{\text{EW}_{\text{line},i}}{\text{FWHM}_{\text{BB}}} S_{\text{BB,line},i}}{\beta + \sum_i \frac{\text{EW}_{\text{line},i}}{\text{FWHM}_{\text{BB}}} S_{\text{NB,line},i}} \frac{f_{\text{NB}}}{f_{\text{BB}}} \quad (\text{A17})$$

where the sum is extended to the number of *features* present in the field stars spectra (equivalent widths would be negative in absorption and positive in emission).

The values determined for β , γ (or the $\beta \times \gamma$ product) would allow to obtain the continuum-subtracted image. However, if we intend to calibrate the resulting image resolving f_{line} in Equation A11 we have to previously derive g_{NB} or g_{BB} . The observation of several spectrophotometric standards stars would allow to obtain the following relation

$$m_{\text{cont},\nu} = ZP - k_{\text{NB}} \sec(z) + 2.5 \log(t_{\text{NB}}) - 2.5 \log(f_{\text{NB}}) \quad (\text{A18})$$

where ZP is the zero point of the calibration, $k_{\lambda,\text{line}}$ is the extinction coefficient for the NB filter, t_{NB} is the exposure time of the NB image, and $m_{\text{cont},\nu}$ is the monochromatic magnitude (see e.g. Hamuy et al. 1992), which is related with the flux via

$$m_{\text{cont},\nu} = -2.5 \log(f_{\text{cont},\nu}) - 48.590 \quad (\text{A19})$$

$$m_{\text{cont},\nu} = -2.5 \log(f_{\text{cont},\lambda}) - 5 \log(\lambda) - 2.398 \quad (\text{A20})$$

where $f_{\text{cont},\nu}$ is expressed in $\text{erg s}^{-1} \text{cm}^{-2} \text{Hz}^{-1}$, $f_{\text{cont},\lambda}$ in $\text{erg s}^{-1} \text{cm}^{-2} \text{\AA}^{-1}$, and λ is in \AA .

Thus, once the ZP and k_{NB} coefficients are obtained from the Bouger-line fit to the spectrophotometric standards data we can obtain the conversion factor g_{NB} from Equations A14, A18, and A20 as

$$g_{\text{NB}} = \frac{f_{\text{NB}}}{f_{\text{cont},\lambda}} \frac{1}{\text{FWHM}_{\text{NB}}} = 10^{0.4(ZP - k_{\text{NB}} \sec(z) + 2.398)} \frac{\lambda^2 t_{\text{NB}}}{\text{FWHM}_{\text{NB}}} \quad (\text{A21})$$

and, then

$$f_{\text{line}} = 10^{-0.4(ZP - k_{\text{NB}} \sec(z) + 2.398)} \frac{\text{FWHM}_{\text{NB}}}{\lambda^2 t_{\text{NB}} \beta \delta} (f_{\text{NB}} - \beta \gamma f_{\text{BB}}) \quad (\text{A22})$$

On the other hand, in the case that only the broad-band image is flux calibrated we obtain

$$m_{\text{BB}} = ZP - k_{\text{BB}} \sec(z) + k_C C + 2.5 \log(t_{\text{BB}}) - 2.5 \log(f_{\text{BB}}) \quad (\text{A23})$$

where k_{BB} is the extinction coefficient for the BB filter, C and k_C are the color and color coefficient for a particular color term, and t_{BB} is the exposure time for the BB image. Since m_{BB} is also expressed as

$$m_{\text{BB}} = m_{\text{BB,Vega}} - 2.5 \log \left(\frac{f_{\text{cont},\lambda}}{f_{\text{cont},\lambda,\text{Vega}}} \right) \quad (\text{A24})$$

we derive g_{BB} using

$$g_{\text{BB}} = \frac{f_{\text{BB}}}{f_{\text{cont},\lambda}} \frac{1}{\text{FWHM}_{\text{BB}}} = 10^{0.4(\text{ZP} - k_{\text{BB}} \sec(z) + k_C C - m_{\text{BB,Vega}})} \frac{t_{\text{BB}}}{f_{\text{cont},\lambda,\text{Vega}} \text{FWHM}_{\text{BB}}}, \quad (\text{A25})$$

which finally leads to the flux of the emission line

$$f_{\text{line}} = 10^{-0.4(\text{ZP} - k_{\text{BB}} \sec(z) + k_C C - m_{\text{BB,Vega}})} \frac{f_{\text{cont},\lambda,\text{Vega}} \text{FWHM}_{\text{BB}}}{t_{\text{BB}} \beta \gamma \delta} (f_{\text{NB}} - \beta \gamma f_{\text{BB}}) \quad (\text{A26})$$

In those cases where both photometric and spectrophotometric calibrators are available the comparison of the $g_{\text{NB}}/g_{\text{BB}}$ ratio with the right side of Equation A16 should provide an additional test for the reliability of the spectral response functions assumed for the NB and BB filters. In our case the differences derived between these two values were of the order of 5 per cent.

Finally, it is important to take into account the contribution that other emission lines could have to the fluxes and equivalent widths derived using Equations A11, A22, A26, and A13. Although the terms due to these other lines (typically the doublet $[\text{NII}]\lambda\lambda 6548, 6584 \text{ \AA}$ for observations in the light of $\text{H}\alpha$) are not included in Equations A1 and A2 their contribution can be corrected by considering that f_{line} , as it appears in these equations, can be defined in a way that

$$S_{\text{NB,line}} f_{\text{line}} \equiv S_{\text{NB,line}} f'_{\text{line}} + \sum_j S_{\text{NB},j} f'_j \quad (\text{A27})$$

where f'_{line} and f'_j are the corrected fluxes for the line of interest and those other lines included in the filter, respectively, and the sum in the index j is extended to all contaminating lines but not the line of study. If we now consider the line ratios between the contaminating lines and the line of interest given by spectroscopy observations,

$$r_j \equiv \frac{f'_j}{f'_{\text{line}}} \quad (\text{A28})$$

we obtain

$$f'_{\text{line}} = \frac{S_{\text{NB,line}}}{S_{\text{NB,line}} + \sum_j S_{\text{NB},j} r_j} f_{\text{line}}. \quad (\text{A29})$$

This expression and the corresponding correction of the EW_{line} are valid as long as the contribution of the contaminating lines to the flux within the BB filter is negligible.

Table 1. Sample

Object Name	RA ₂₀₀₀ (h m s)	DEC ₂₀₀₀ (° ' ")	A _B (mag)	v _{helio} (km/s)	λ _{Hα} (Å)	Hα filter	Distance (Mpc)	[NII]/Hα
(1)	(2)	(3)	(4)	(5)	(6)	(7)	(8)	(9)
IC 10 ⁽¹⁾	00 20 17.3	+59 18 14	6.16	-348	6555.2	PO 6563	1.0	0.045
HS 0029+1748	00 32 03.1	+18 04 46	0.57	2188	6610.7	PO 6614	33.3	0.055:
Haro 14	00 45 46.4	-15 35 49	0.09	944	6583.5	PO 6584	14.0	0.093
UM 285	00 51 58.8	-01 40 18	0.24	1900	6604.4	PO 6601	28.2	0.055:
UCM 0049-0045	00 51 59.6	-00 29 12	0.17	1633	6598.5	PO 6593	24.4	0.055:
UM 323	01 26 46.6	-00 38 46	0.13	1923	6604.9	PO 6601	28.3	0.055:
Mrk 996	01 27 35.5	-06 19 36	0.19	1622	6598.3	PO 6593	23.7	0.057
UM 133	01 44 41.3	+04 53 26	0.16	1623	6598.3	PO 6593	24.1	0.055:
UM 382	01 58 09.4	-00 06 38	0.12	3526	6639.9	PO 6640	50.9	0.055:
UM 404	02 10 12.2	-01 24 49	0.15	3598	6641.6	PO 6640	51.8	0.055:
KUG 0207-016A	02 10 09.8	-01 24 03	0.15	3523	6639.9	PO 6640	50.7	0.055:
UM 408	02 11 23.5	+02 20 31	0.15	3598	6641.6	PO 6640	51.9	0.039
UM 417	02 19 30.3	-00 59 13	0.14	2698	6621.9	PO 6614	38.9	0.055:
Mrk 370	02 40 29.0	+19 17 50	0.40	790	6580.1	PO 6584	12.2	0.055:
Mrk 600	02 51 04.6	+04 27 14	0.28	1008	6584.9	PO 6584	14.6	0.025
NGC 1522	04 06 07.7	-52 40 09	0.06	905	6582.6	LC 6570	10.6	0.055:
NGC 1705 ⁽²⁾	04 54 13.7	-53 21 41	0.04	628	6576.5	LC 6570	5.1	0.055:
II Zw 33	05 10 48.1	-02 43 00	0.45	2850	6625.2	PO 6624	39.4	0.070
II Zw 33B	05 10 45.2	-02 45 31	0.44	2870	6625.6	PO 6624	39.7	0.055:
II Zw 40	05 55 42.8	+03 23 30	3.54	789	6580.1	PO 6584	9.8	0.024
Tol 0610-387	06 12 13.7	-38 46 26	0.33	1799	6602.2	LC 6600	22.8	0.055:
Mrk 0005	06 42 15.5	+75 37 33	0.36	792	6580.1	PO 6584	13.2	0.058
Mrk 0007	07 28 12.0	+72 34 29	0.13	3060	6629.8	PO 6624	45.4	0.055:
Mrk 86 ⁽³⁾	08 13 14.7	+45 59 26	0.23	447	6572.6	PO 6570	6.9	0.154
HS 0822+3542	08 25 55.4	+35 32 32	0.20	732	6578.8	PO 6584	10.1	0.005
UGC 4483 ⁽⁴⁾	08 37 03.0	+69 46 50	0.15	178	6566.7	PO 6563	3.2	0.055:
UGC 4703N1	08 58 29.8	+06 19 17	0.30	3551	6640.5	LC 6630	48.8	0.151
UGC 4703N2	08 58 27.4	+06 20 06	0.29	3536	6640.2	LC 6630	48.6	0.151
Mrk 1416	09 20 56.2	+52 34 05	0.07	2326	6613.7	PO 6614	33.8	0.055:
Mrk 108	09 21 30.3	+64 14 20	0.24	1534	6596.4	PO 6593	21.8	0.032
Mrk 400	09 26 01.2	+19 23 01	0.15	2522	6618.0	PO 6614	34.8	0.055:

Table 1—Continued

Object Name	RA ₂₀₀₀ (h m s)	DEC ₂₀₀₀ (° ' ")	A _B (mag)	v _{helio} (km/s)	λ _{Hα} (Å)	Hα filter	Distance (Mpc)	[NII]/Hα
(1)	(2)	(3)	(4)	(5)	(6)	(7)	(8)	(9)
NGC 2915 ⁽⁵⁾	09 26 11.5	−76 37 36	1.18	468	6573.0	LC 6570	3.6	0.055:
I Zw 18 ⁽⁶⁾	09 34 02.0	+55 14 28	0.14	751	6579.2	PO 6584	12.6	0.016
Mrk 1418	09 40 27.1	+48 20 15	0.10	773	6579.7	PO 6584	11.4	0.055:
Mrk 1423	09 43 01.6	+58 58 25	0.07	1358	6592.5	PO 6593	20.4	0.055:
SBS 0940+544C	09 44 16.7	+54 11 33	0.05	1638	6598.7	PO 6593	24.1	0.006
Mrk 709	09 49 18.0	+16 52 46	0.15	1197	6589.0	PO 6593	15.7	0.098
Mrk 1426	09 49 18.3	+48 33 50	0.06	1835	6602.9	PO 6601	26.6	0.055:
UGCA 184	09 49 30.4	+55 34 49	0.04	1551	6596.8	PO 6593	23.0	0.023
Mrk 409	09 49 41.2	+32 13 16	0.07	1527	6596.2	PO 6593	21.3	0.055:
Tol 001	09 56 14.9	−29 36 21	0.40	1839	6603.0	LC 6600	23.2	0.055:
Tol 002	09 59 20.7	−28 07 54	0.40	710	6578.3	LC 6570	7.1	0.047
NGC 3125	10 06 33.6	−29 56 09	0.33	865	6581.7	LC 6570	9.3	0.030
SBS 1006+578	10 09 55.0	+57 36 00	0.04	1512	6595.9	PO 6593	22.5	0.055:
Haro 2	10 32 31.9	+54 24 03	0.05	1461	6594.8	PO 6593	21.6	0.220
Mrk 1434	10 34 10.1	+58 03 49	0.03	2269	6612.5	PO 6614	33.4	0.055:
Haro 3	10 45 22.4	+55 57 37	0.03	944	6583.5	PO 6584	14.4	0.063
SBS 1054+504	10 56 58.7	+50 08 26	0.07	1358	6592.5	PO 6593	20.1	0.055:
Haro 4	11 04 58.5	+29 08 22	0.13	646	6576.9	PO 6570	8.8	0.018
VII Zw 403 ⁽⁷⁾	11 27 59.9	+78 59 39	0.16	−100	6560.6	PO 6563	4.8	0.055:
Mrk 178 ⁽⁸⁾	11 33 29.1	+49 14 17	0.08	249	6568.3	PO 6563	4.2	0.021
UM 439	11 36 36.9	+00 49 01	0.11	1099	6586.8	PO 6584	14.0	0.015
Mrk 1450	11 38 35.6	+57 52 27	0.04	946	6583.5	PO 6584	14.7	0.025
UM 452	11 47 00.7	−00 17 39	0.14	1478	6595.1	PO 6593	19.5	0.100
SBS 1147+520	11 49 54.4	+51 44 11	0.10	1257	6590.3	PO 6593	18.9	0.055:
Tol 17	11 50 03.0	−28 40 17	0.33	2099	6608.7	LC 6600	27.4	0.050
UM 455	11 50 23.7	−00 31 43	0.11	3863	6647.3	LC 6630	53.6	0.055:
UM 456	11 50 36.2	−00 34 02	0.12	1757	6601.2	LC 6600	23.5	0.055:
UM 456A	11 50 34.0	−00 32 16	0.12	1831	6602.9	LC 6600	24.5	0.055:
Pox 4	11 51 11.6	−20 36 02	0.17	3589	6641.3	LC 6630	48.9	0.014
ESO 572-G025	11 57 28.0	−19 37 27	0.21	1781	6601.8	LC 6600	23.1	0.055:
VCC 0001 ⁽⁹⁾	12 08 20.3	+13 41 03	0.14	2267	6612.4	PO 6614	16.0	0.055:

Table 1—Continued

Object Name	RA ₂₀₀₀ (h m s)	DEC ₂₀₀₀ (° ' ")	A _B (mag)	v _{helio} (km/s)	λ _{Hα} (Å)	Hα filter	Distance (Mpc)	[NII]/Hα
(1)	(2)	(3)	(4)	(5)	(6)	(7)	(8)	(9)
Mrk 1313	12 12 14.7	+00 04 20	0.11	2328	6613.8	PO 6614	31.8	0.030
VCC 0130 ⁽⁹⁾	12 15 04.0	+09 45 13	0.07	2189	6610.7	LC 6600	16.0	0.055:
Haro 8 ⁽⁹⁾	12 19 09.9	+03 51 21	0.07	1526	6596.2	PO 6593	16.0	0.055:
UM 491	12 19 53.1	+01 46 24	0.10	2025	6607.1	PO 6601	27.6	0.055:
ISZ 399	12 19 59.5	−17 23 31	0.25	900	6582.5	LC 6570	10.8	0.055:
VCC 0459 ⁽⁹⁾	12 21 11.2	+17 38 18	0.15	2107	6608.9	LC 6600	16.0	0.055:
VCC 0655 ⁽⁹⁾	12 23 37.5	+17 32 27	0.15	1142	6587.8	LC 6600	16.0	0.055:
Tol 65	12 25 46.9	−36 14 01	0.32	2698	6621.8	LC 6630	36.0	0.007
VCC 0848 ⁽⁹⁾	12 25 52.5	+05 48 33	0.10	1537	6596.4	LC 6600	16.0	0.055:
Mrk 209 ⁽¹⁰⁾	12 26 16.0	+48 29 37	0.06	281	6569.0	PO 6563	5.8	0.010
Mrk 1329 ⁽⁹⁾	12 37 03.0	+06 55 36	0.10	1632	6598.5	PO 6593	16.0	0.026
UGCA 290 ⁽¹¹⁾	12 37 21.8	+38 44 38	0.06	445	6572.5	PO 6570	6.7	0.055:
VCC 1750 ⁽⁹⁾	12 38 15.5	+06 59 39	0.09	−117	6560.2	LC 6570	16.0	0.055:
Haro 9	12 45 17.1	+27 07 32	0.06	1069	6586.2	PO 6584	15.3	0.220
NGC 4861	12 59 01.8	+34 51 40	0.04	847	6581.3	PO 6584	12.6	0.042
UM 533	12 59 58.1	+02 02 59	0.11	886	6582.2	PO 6584	11.7	0.055:
Mrk 450	13 14 48.3	+34 52 51	0.06	863	6581.7	PO 6584	13.0	0.038
NGC 5058	13 16 52.3	+12 32 55	0.13	961	6583.8	PO 6584	13.4	0.055:
PGC 046448	13 19 22.2	−15 09 24	0.28	2832	6624.8	LC 6630	38.9	0.055:
Pox 186	13 25 48.6	−11 36 38	0.20	1170	6588.4	LC 6600	15.4	0.055:
Tol 35	13 27 06.5	−27 57 24	0.23	2023	6607.1	LC 6600	27.0	0.038
SBS 1331+493	13 33 22.9	+49 06 06	0.04	599	6575.9	PO 6570	9.9	0.037
Tol 85	13 37 08.2	−32 55 28	0.23	3598	6641.5	LC 6630	49.4	0.055:
Mrk 67	13 41 56.5	+30 31 10	0.08	958	6583.8	PO 6584	14.3	0.019
Mrk 1480	13 42 51.8	+52 42 31	0.05	1798	6602.2	PO 6601	27.2	0.055:
Mrk 1481	13 42 59.3	+52 41 18	0.04	1803	6602.3	PO 6601	27.3	0.055:
Tol 1345-420	13 48 22.2	−42 21 15	0.43	2398	6615.3	LC 6600	32.1	0.018
HS 1400+3927	14 02 36.1	+39 13 13	0.06	1396	6593.4	PO 6593	21.1	0.055:
SBS 1415+437	14 17 01.7	+43 30 13	0.04	609	6576.1	PO 6570	10.1	0.013
SBS 1428+457	14 30 12.2	+45 32 32	0.05	2360	6614.5	PO 6614	35.3	0.055:
Tol 1434+032	14 37 19.4	+03 03 01	0.15	1499	6595.6	PO 6593	21.4	0.055:

Table 1—Continued

Object Name	RA ₂₀₀₀ (h m s)	DEC ₂₀₀₀ (° ' ")	A _B (mag)	v _{helio} (km/s)	λ _{Hα} (Å)	Hα filter	Distance (Mpc)	[NII]/Hα
(1)	(2)	(3)	(4)	(5)	(6)	(7)	(8)	(9)
Mrk 475	14 39 05.4	+36 48 21	0.05	583	6575.6	PO 6570	9.7	0.055:
HS 1440+4302	14 42 15.9	+42 49 48	0.06	2548	6618.6	PO 6614	38.0	0.038
HS 1442+4250	14 44 12.1	+42 37 37	0.06	749	6579.2	PO 6584	12.3	0.055:
UCM 1446+2312	14 48 45.2	+22 59 34	0.14	2398	6615.3	PO 6614	35.2	0.055:
Tol 1448+116	14 50 22.7	+11 24 11	0.10	1870	6603.7	PO 6601	27.2	0.055:
II Zw 70	14 50 56.5	+35 34 18	0.05	1215	6589.4	PO 6593	18.7	0.048
II Zw 71	14 51 14.4	+35 32 31	0.06	1292	6591.1	PO 6593	18.7	0.114
I Zw 115	15 32 57.0	+46 27 07	0.06	656	6577.2	PO 6570	11.4	0.055:
SBS 1533+574	15 34 13.8	+57 17 06	0.06	3310	6635.3	PO 6640	49.6	0.055:
I Zw 123	15 37 04.2	+55 15 48	0.06	665	6577.4	PO 6570	11.7	0.033
HS 1609+4827	16 11 11.5	+48 20 04	0.06	2817	6624.5	PO 6624	42.6	0.055:
UCM 1612+1308	16 15 17.1	+13 01 32	0.21	3630	6642.3	PO 6640	53.2	0.026
UGCA 412	16 35 21.1	+52 12 53	0.12	2700	6621.9	PO 6624	41.1	0.055:
HS 1704+4332	17 05 45.4	+43 28 49	0.13	2076	6608.2	PO 6614	32.2	0.055:
NGC 6789 ⁽¹²⁾	19 16 41.9	+63 58 18	0.30	-141	6559.7	PO 6563	3.6	0.055:
Tol 1924-416	19 27 58.2	-41 34 32	0.38	2874	6625.7	LC 6630	41.0	0.024
Tol 1937-423	19 40 58.1	-42 15 44	0.34	2698	6621.8	LC 6630	41.8	0.055:
Mrk 900	21 29 59.6	+02 24 51	0.24	1152	6588.0	PO 6584	18.8	0.131
Mrk 314	23 02 59.2	+16 36 19	0.38	2081	6608.4	PO 6614	32.2	0.055:
Mrk 324	23 26 32.8	+18 15 59	0.22	1600	6597.8	PO 6593	25.3	0.051
Mrk 328	23 37 39.6	+30 07 47	0.40	1379	6593.0	PO 6593	22.4	0.221

Note. — Columns stand for: (1) Galaxy name. (2) Right Ascension (J2000) in (h m s). (3) Declination (J2000) in (° ' "). (4) *B*-band Galactic extinction in magnitudes (Schelegel et al. 1998) . (5) Heliocentric radial velocity in km s⁻¹ (taken from NED). (6) Observed wavelength for Hα (Å). (7) Filter used for the Hα-line imaging. (8) Distance (Mpc). (9) [NII]λ6584 Å/Hα intensity ratio. Values of 0.055: are estimated values only, adopted from the average of 49 other galaxies in the sample.

References. — For non-redshift distances: (1) Hunter (2001); (2) Tosi et al. (2001); (3) Sharina, Karachentsev, & Tikhonov (1999); (4) Dolphin et al. (2001); (5) Meurer et al. (1996); (6) Östlin (2000); (7) Schulte-Ladbeck et al. (1999); (8) Schulte-Ladbeck et al. (2000); (9) Virgo cluster (Macri et al. 1999); (10) Schulte-Ladbeck et al. (2001); (11) Crone et al. (2000); (12) Drozdovsky et al. (2001).

Table 2. Observing runs

Run	Nights	Observatory	Telescope	Detector	Scale ("/pix)	Gain (e ⁻ /ADU)	RN (e ⁻)
(1)	(2)	(3)	(4)	(5)	(6)	(7)	(8)
Jun01	06-09	Palomar	60"	CCD#13	0.378	1.6	6.3
Sep01	10-12	Palomar	60"	CCD#13	0.378	1.6	6.3
Nov01	08-09	Palomar	60"	CCD#13	0.378	1.6	6.3
Dec01	04-09	Palomar	60"	CCD#13	0.378	1.6	6.3
Jan02	14-16	Palomar	60"	CCD#13	0.378	1.6	6.3
Jan02B	20-23	Palomar	60"	CCD#13	0.378	1.6	6.3
Feb02	08-09	Las Campanas	100"	Tek5	0.260	2.0	6.6
Mar02	05-09	Las Campanas	100"	Tek5	0.260	3.0	7.0
Mar02B	14-19	Palomar	60"	CCD#13	0.378	1.6	6.3
May02	13-16	Palomar	60"	CCD#13	0.378	1.6	6.3
Jul02	01-08	Palomar	60"	CCD#13	0.378	1.6	6.3

Note. — Columns stand for: (1) Observing run. (2) Nights observed. (3) Observatory. (4) Telescope. (5) Detector. (6) Spatial scale at the detector in arcsec/pixel. (8) Gain of the detector in e⁻/ADU. (9) Readout noise of the detector in e⁻. Note that two different gain settings were used during the Las Campanas observing runs.

Table 3. Images (abridged)

Object Name	Tel	<i>B</i> -band				<i>R</i> -band				$H\alpha$			
		Date	t_{exp} (s)	X	PSF (")	Date	t_{exp} (s)	X	PSF (")	Date	t_{exp} (s)	X	PSF (")
(1)	(2)	(3)	(4)	(5)	(6)	(7)	(8)	(9)	(10)	(11)	(12)	(13)	(14)
IC 10	P60	01/20/02	1×900	1.24	2.5	12/06/01	3×900	1.12	1.8	12/06/01	3×1500	1.12	1.8
HS 0029+1748	P60	12/07/01	1×900	1.08	3.5	11/08/01	3×600	1.05	1.5	11/08/01	2×1800	1.15	1.5
Haro 14	P60	12/07/01	1×900	1.55	4.3	09/11/01	3×600	1.66	1.9	09/11/01	3×1800	1.53	1.8
UM 285	P60	07/07/02	1×900	1.70	2.0	07/05/02	3×600	1.66	1.7	07/05/02	3×1200	1.45	1.8
UCM 0049-0045	P60	01/21/02	1×900	1.48	3.2	01/14/02	1×900	1.40	3.6	01/14/02	2×1200	1.55	2.9
UM 323	P60	07/07/02	1×300	1.64	2.2	07/03/02	3×600	1.75	1.9	07/03/02	2×1500	1.60	2.0
Mrk 996	P60	12/04/01	1×900	1.32	3.3	09/12/01	3×600	1.57	1.6	09/12/01	3×1800	1.35	1.4
UM 133	P60	07/07/02	1×900	1.73	2.3	07/06/02	1×600	1.75	1.5	07/01/02	3×1200	1.85	2.6
UM 382	P60	12/04/01	1×900	1.24	2.4	11/09/01	3×600	1.25	1.1	11/09/01	2×1800	1.21	1.2
UM 404	P60	12/07/01	2×900	1.29	3.8	12/05/01	3×900	1.56	2.5	12/05/01	3×1800	1.28	1.7

Note. — Columns stand for: (1) Galaxy name. (2) Observatory and telescope (P60: Palomar Observatory 60-inch; C100: Las Campanas observatory du Pont 100-inch). (3) Date of observation for the *B*-band image. (4) Number of frames and exposure time per frame for the *B*-band in seconds. (5) Mean airmass of the *B*-band exposure. (6) Seeing (FWHM) of the *B*-band image in arcsec. (7-10) The same as (3-6) for the *R*-band exposure. (11-14) The same as (3-6) for the $H\alpha$ exposure.

Table 4. Calibration results

Night	Telescope	Band	C_λ (mag)	k_λ (mag/am)	$k_{\lambda,B-R}$	rms (mag)	N	Notes
(1)	(2)	(3)	(4)	(5)	(6)	(7)	(8)	(9)
12/04/01	P60	B	23.760	0.264	+0.035	0.03	49	
	P60	R	23.787	0.120	−0.051	0.01	34	
12/07/01	P60	B	23.769	0.250	+0.050	0.05	11	(a)
	P60	R	23.796	0.110	−0.050	0.04	12	(a)
01/20/02	P60	B	23.717	0.225	+0.052	0.03	25	
	P60	R	23.762	0.104	−0.046	0.02	22	
01/21/02	P60	B	23.674	0.202	+0.069	0.04	15	
	P60	R	23.793	0.116	−0.050	0.08	12	(b)
02/08/02	C100	B	24.960	0.298	+0.050	0.01	10	
	C100	R	24.942	0.192	−0.050	0.06	6	(b)
	C100	H α 6570	21.903	0.110		0.01	3	(a)
03/05/02	C100	B	24.390	0.187	+0.050	0.05	4	(b)
	C100	R	24.341	0.074	−0.050	0.01	4	(b)
	C100	H α 6600	21.446	0.110		0.02	4	(a)
03/06/02	C100	B	24.491	0.250	+0.050	0.04	3	(a)
	C100	R	24.398	0.110	−0.050	0.03	3	(a)
	C100	H α 6600	21.448	0.110		0.03	3	(a)
	C100	H α 6630	21.512	0.110		0.02	3	(a)
03/09/02	C100	B	24.342	0.225	+0.050	0.03	4	(b)
	C100	R	24.335	0.110	−0.050	0.01	4	(a)
	C100	H α 6600	21.430	0.117		0.04	5	(b)
	C100	H α 6630	21.472	0.089		0.05	4	(b)
03/14/02	P60	B	23.745	0.287	+0.074	0.04	32	
	P60	R	23.755	0.114	−0.035	0.05	37	
05/15/02	P60	B	23.718	0.266	+0.054	0.03	29	
	P60	R	23.745	0.114	−0.059	0.02	30	
07/07/02	P60	B	23.886	0.286	+0.047	0.03	30	
	P60	R	23.829	0.113	−0.055	0.03	28	
07/08/02	P60	B	23.853	0.347	+0.080	0.05	37	
	P60	R	23.825	0.154	−0.042	0.05	40	

Note. — (a) Both the extinction coefficient and the color term are fixed. (b) The color term is fixed. Columns stand for: (1) Date corresponding to the civil time at the start of the observing night. (2) Observatory and telescope (P60: Palomar Observatory 60-inch; C100: Las Campanas Observatory du Pont 100-inch). (3) Band. (4) Photometric zero point in magnitudes. (5) Extinction coefficient in mag/airmass. (6) $B - R$ color coefficient. (7) RMS of the calibration. (8) Number of standard stars used in the fit. (9) Notes.

Table 5. Integrated Photometry

Object Name	B	R	B-R	$f_{\text{H}\alpha}$	M_B	$\log L_{\text{H}\alpha}$	T	$\text{EW}_{\text{H}\alpha}$
	(mag)	(mag)	(mag)	(10^{-14} erg/s/cm 2)	(mag)	(erg/s)		(Å)
(1)	(2)	(3)	(4)	(5)	(6)	(7)	(8)	(9)
IC 10	5.75±0.03	5.45±0.08	0.30±0.08	51000±3700	-19.25	40.79	iI,C	36
HS 0029+1748	16.74±0.05	15.93±0.14	0.81±0.15	19.1±2.5	-15.87	40.40	nE	228
Haro 14	13.65±0.05	12.91±0.14	0.74±0.15	34±4	-17.08	39.90	iE	22
UM 285	17.00±0.03	17.03±0.08	-0.02±0.08	5.8±0.4	-15.25	39.74	iI,C	187
UCM 0049-0045	14.76±0.04	13.36±0.25	1.39±0.25	20±4	-17.18	40.14	iE	20
UM 323	16.09±0.04	15.24±0.08	0.85±0.09	14.1±1.2	-16.17	40.13	iE	83
Mrk 996	15.01±0.03	14.08±0.14	0.93±0.14	54±7	-16.87	40.56	nE	109
UM 133	15.41±0.03	14.51±0.14	0.90±0.14	20±3	-16.50	40.15	iI,C	60
UM 382	18.20±0.04	17.83±0.22	0.37±0.22	2.6±0.5	-15.33	39.90	iI,C	170
UM 404	18.48±0.05	18.40±0.12	0.08±0.13	3.6±0.4	-15.09	40.06	i0	455
KUG 0207-016A	15.24±0.05	14.77±0.12	0.47±0.13	14.3±1.5	-18.28	40.64	iI	54
UM 408	17.46±0.16	16.70±0.12	0.75±0.20	6.8±0.8	-16.12	40.34	nE	161
UM 417	18.37±0.07	17.73±0.13	0.64±0.15	4.4±0.5	-14.58	39.90	iI,C	279
Mrk 370	13.49±0.03	12.21±0.12	1.28±0.13	70±7	-16.94	40.10	iE	24
Mrk 600	14.85±0.03	14.82±0.15	0.03±0.15	24±3	-15.97	39.78	iE	96
NGC 1522	14.03±0.01	13.22±0.06	0.81±0.06	59.9±0.6	-16.10	39.91	iE	54
NGC 1705	13.09±0.01	12.19±0.06	0.90±0.06	253±3	-15.45	39.90	iE	90
II Zw 33	14.21±0.03	13.34±0.11	0.86±0.11	93±9	-18.77	41.24	iI	95
II Zw 33B	16.87±0.04	15.67±0.11	1.21±0.12	5.1±0.5	-16.12	39.98	iI	43
II Zw 40	11.87±0.04	11.10±0.09	0.77±0.09	1554±120	-18.09	41.25	iI,M	217
Tol 0610-387	15.90±0.05	14.87±0.06	1.03±0.08	16±1	-15.89	40.01	iE	68
Mrk 005	15.13±0.04	14.56±0.13	0.57±0.13	28±3	-15.47	39.77	iI,C	89
Mrk 007	14.29±0.03	13.49±0.18	0.79±0.18	36±6	-19.00	40.95	iI	41
Mrk 86	12.07±0.03	11.49±0.11	0.58±0.11	241±23	-17.13	40.14	iE,r	44
HS 0822+3542	17.85±0.03	17.76±0.14	0.09±0.14	7.4±0.9	-12.18	38.95	iI,C	546
UGC 4483	15.14±0.03	14.56±0.13	0.58±0.13	36±4	-12.38	38.64	iI,C	115
UGC 4703N1	15.86±0.04	15.01±0.03	0.85±0.05	24.9±0.5	-17.58	40.85	iI,M	120
UGC 4703N2	17.04±0.04	16.10±0.03	0.94±0.05	...	-16.39
Mrk 1416	16.32±0.03	15.75±0.02	0.58±0.04	19.4±0.8	-16.32	40.42	iI	191
Mrk 108	15.15±0.03	14.66±0.08	0.49±0.08	73±5	-16.54	40.62	iI,M	275
Mrk 400	14.30±0.04	13.63±0.11	0.67±0.12	39±4	-18.41	40.76	iE,r	51

Table 5—Continued

Object Name	B	R	B-R	$f_{\text{H}\alpha}$	M_B	$\log L_{\text{H}\alpha}$	T	$\text{EW}_{\text{H}\alpha}$
	(mag)	(mag)	(mag)	(10^{-14} erg/s/cm ²)	(mag)	(erg/s)		(Å)
(1)	(2)	(3)	(4)	(5)	(6)	(7)	(8)	(9)
NGC 2915	11.93±0.01	10.96±0.06	0.97±0.06	209±3	-15.85	39.51	iE	23
I Zw 18	16.05±0.04	16.24±0.07	-0.18±0.08	35.2±2.4	-14.45	39.83	i0	679
Mrk 1418	13.86±0.03	12.61±0.19	1.25±0.20	95±16	-16.42	40.17	iE	49
Mrk 1423	14.90±0.03	13.52±0.10	1.38±0.11	6.8±0.4	-16.65	39.53	nE	8
SBS 0940+544C	17.18±0.04	17.05±0.10	0.13±0.11	5.1±0.5	-14.73	39.55	iI,M	165
Mrk 709	16.32±0.03	15.65±0.02	0.67±0.04	...	-14.66
Mrk 1426	15.88±0.04	15.44±0.12	0.44±0.12	7.8±0.8	-16.24	39.82	iE	55
UGCA 184	15.99±0.04	15.80±0.10	0.19±0.11	14.0±1.4	-15.82	39.95	iI	142
Mrk 409	14.37±0.03	13.33±0.05	1.04±0.06	29.2±1.7	-17.27	40.20	iE,r	29
Tol 001	15.74±0.05	15.48±0.07	0.26±0.09	12.0±0.9	-16.09	39.89	iE	88
Tol 002	14.06±0.01	13.34±0.06	0.72±0.06	121.3±1.8	-15.19	39.86	iE	127
NGC 3125	13.05±0.01	12.25±0.06	0.80±0.06	342±4	-16.79	40.55	iE	131
SBS 1006+578	16.42±0.04	15.78±0.11	0.64±0.12	5.6±0.6	-15.34	39.53	iE	53
Haro 2	13.39±0.04	12.87±0.11	0.52±0.11	157±16	-18.28	40.94	nE	105
Mrk 1434	16.77±0.04	16.43±0.13	0.33±0.14	16.4±2.0	-15.85	40.34	i0	324
Haro 3	13.22±0.04	12.61±0.13	0.61±0.14	275±30	-17.57	40.83	iE	148
SBS 1054+504	16.08±0.04	15.46±0.15	0.62±0.15	4.3±0.5	-15.44	39.32	nE	30
Haro 4	15.59±0.04	15.44±0.17	0.15±0.17	66±12	-14.14	39.79	iI	589
VII Zw 403	14.11±0.04	13.58±0.11	0.53±0.12	59±6	-14.30	39.21	iE	75
Mrk 178	14.15±0.04	13.60±0.09	0.55±0.10	109±9	-13.96	39.36	iI,M	146
UM 439	14.77±0.03	14.09±0.06	0.67±0.07	42.8±2.5	-15.96	40.00	iE	88
Mrk 1450	15.75±0.05	15.09±0.09	0.67±0.10	42±4	-15.08	40.04	nE	234
UM 452	15.25±0.03	14.07±0.11	1.19±0.12	4.7±0.5	-16.20	39.33	nE	9
SBS 1147+520	16.95±0.05	15.98±0.09	0.97±0.10	1.4±0.2	-14.44	38.78	nE	16
Tol 17	15.99±0.05	15.05±0.06	0.94±0.08	17.5±1.0	-16.20	40.20	iE	86
UM 455	17.02±0.03	16.26±0.01	0.77±0.03	6.9±0.3	-16.62	40.38	iI	105
UM 456	15.37±0.03	14.66±0.01	0.71±0.03	24.5±0.9	-16.48	40.21	iI	85
UM 456A	16.71±0.03	16.05±0.01	0.66±0.03	4.20±0.16	-15.24	39.48	iI	51
Pox 4	15.27±0.04	14.88±0.10	0.38±0.11	94±9	-18.18	41.43	iI,M	478
ESO 572-G025	15.02±0.04	14.07±0.03	0.94±0.05	60.6±1.6	-16.80	40.59	nE	125
VCC 0001	15.80±0.03	14.42±0.01	1.37±0.04	1.90±0.06	-15.22	38.77	nE	5

Table 5—Continued

Object Name	B	R	B-R	$f_{H\alpha}$	M_B	$\log L_{H\alpha}$	T	$EW_{H\alpha}$
	(mag)	(mag)	(mag)	(10^{-14} erg/s/cm ²)	(mag)	(erg/s)		(Å)
(1)	(2)	(3)	(4)	(5)	(6)	(7)	(8)	(9)
Mrk 1313	16.02±0.03	15.50±0.06	0.52±0.06	8.6±0.5	-16.49	40.02	i0	64
VCC 0130	17.05±0.05	16.27±0.01	0.78±0.05	1.75±0.06	-13.97	38.73	iE	26
Haro 8	14.27±0.03	13.20±0.11	1.07±0.11	43±4	-16.75	40.12	nE	38
UM 491	15.54±0.03	14.95±0.07	0.59±0.08	8.8±0.6	-16.66	39.90	nE	39
ISZ 399	14.18±0.01	12.99±0.06	1.19±0.06	41.8±2.4	-15.99	39.77	nE	30
VCC 0459	14.95±0.05	14.13±0.01	0.83±0.05	20.4±0.5	-16.07	39.80	iI	42
VCC 0655	13.32±0.04	12.12±0.03	1.20±0.05	75.1±2.2	-17.70	40.36	iE,r	24
Tol 65	17.26±0.04	16.84±0.03	0.42±0.05	24.9±1.0	-15.52	40.59	i0	916
VCC 0848	15.03±0.05	14.10±0.01	0.93±0.05	14.2±0.4	-15.99	39.64	iI,M	28
Mrk 209	14.15±0.03	13.94±0.13	0.21±0.13	173±20	-14.67	39.84	iE	349
Mrk 1329	14.08±0.03	13.38±0.09	0.70±0.10	67±6	-16.94	40.31	iI,C	70
UGCA 290	15.67±0.03	15.04±0.13	0.63±0.13	6.2±0.9	-13.46	38.52	iI,M	29
VCC 1750	16.73±0.03	15.93±0.05	0.80±0.06	3.8±0.2	-14.29	39.06	iI	41
Haro 9	13.02±0.05	12.24±0.10	0.78±0.11	221±21	-17.91	40.79	nE	82
NGC 4861	12.68±0.03	11.91±0.09	0.76±0.09	560±5	-17.82	41.03	iI,C	160
UM 533	14.63±0.04	13.64±0.11	0.99±0.11	31±3	-15.71	39.71	iE	41
Mrk 450	14.44±0.05	13.65±0.10	0.79±0.11	11.8±1.1	-16.13	39.38	iE	15
NGC 5058	14.05±0.03	13.37±0.07	0.68±0.08	45±3	-16.58	39.99	iI	47
PGC 046448	15.47±0.03	14.51±0.01	0.96±0.03	8.9±0.4	-17.48	40.21	iE	26
Pox 186	17.73±0.03	17.39±0.01	0.35±0.04	14.8±0.5	-13.20	39.62	i0	907
Tol 35	14.17±0.03	13.22±0.05	0.94±0.06	83±4	-17.99	40.86	iE	76
SBS 1331+493	14.87±0.03	14.16±0.17	0.71±0.17	25±4	-15.11	39.47	iE	54
Tol 85	16.51±0.03	15.99±0.01	0.52±0.03	20.5±0.9	-16.96	40.78	iI	261
Mrk 67	16.10±0.03	15.34±0.08	0.76±0.09	25.1±2.0	-14.67	39.79	nE	170
Mrk 1480	16.17±0.03	15.56±0.08	0.61±0.08	13.9±1.0	-16.01	40.09	nE	111
Mrk 1481	16.19±0.03	15.57±0.06	0.62±0.07	4.4±0.3	-15.99	39.60	iI,M	34
Tol 1345-420	15.87±0.03	15.00±0.03	0.87±0.05	33.5±1.1	-16.67	40.62	nE	165
HS 1400+3927	17.04±0.05	15.94±0.10	1.10±0.12	8.6±0.8	-14.58	39.66	nE	97
SBS 1415+437	15.43±0.03	14.77±0.12	0.66±0.13	50±6	-14.59	39.79	iI,C	203
SBS 1428+457	15.42±0.05	14.67±0.09	0.75±0.10	48±4	-17.32	40.85	iI	173
Tol 1434+032	15.86±0.03	15.42±0.06	0.44±0.07	11.3±0.7	-15.80	39.79	iI	78

Table 5—Continued

Object Name	B	R	B-R	$f_{\text{H}\alpha}$	M_B	$\log L_{\text{H}\alpha}$	T	$\text{EW}_{\text{H}\alpha}$
	(mag)	(mag)	(mag)	(10^{-14} erg/s/cm 2)	(mag)	(erg/s)		(Å)
(1)	(2)	(3)	(4)	(5)	(6)	(7)	(8)	(9)
Mrk 475	16.20±0.03	15.67±0.07	0.53±0.08	35.6±2.4	-13.73	39.60	nE	355
HS 1440+4302	17.58±0.05	16.54±0.11	1.04±0.12	4.1±0.4	-15.32	39.85	nE	80
HS 1442+4250	15.55±0.05	15.01±0.07	0.54±0.09	14.7±1.1	-14.90	39.42	iE	69
UCM 1446+2312	15.77±0.03	14.52±0.09	1.25±0.10	...	-16.96
Tol 1448+116	16.15±0.05	15.95±0.10	0.21±0.12	8.9±0.9	-16.02	39.90	iE	101
II Zw 70	14.84±0.12	14.29±0.13	0.55±0.18	83±11	-16.52	40.54	iI	217
II Zw 71	14.45±0.15	13.54±0.12	0.91±0.19	40±4	-16.91	40.23	iI	49
I Zw 115	15.04±0.09	14.14±0.08	0.91±0.12	1.88±0.16	-15.24	38.47	iE	4
SBS 1533+574	16.02±0.10	15.30±0.10	0.72±0.14	30±3	-17.46	40.95	iE	198
I Zw 123	15.42±0.10	14.85±0.08	0.57±0.13	35±3	-14.92	39.76	nE	151
HS 1609+4827	15.11±0.11	14.55±0.09	0.56±0.14	20.9±1.8	-18.04	40.66	nE	64
UCM 1612+1308	17.21±0.14	17.31±0.07	-0.10±0.15	7.1±0.5	-16.42	40.38	i0	313
UGCA 412	15.55±0.05	14.62±0.09	0.92±0.11	35±3	-17.52	40.85	nE	120
HS 1704+4332	18.41±0.03	17.87±0.08	0.54±0.09	3.3±0.3	-14.13	39.61	i0	236
NGC 6789	13.74±0.03	12.69±0.07	1.05±0.08	32.7±2.0	-14.04	38.70	iE	18
Tol 1924-416	13.97±0.04	13.50±0.03	0.47±0.05	297±5	-19.09	41.78	iE	413
Tol 1937-423	15.14±0.04	14.25±0.03	0.89±0.05	21.7±0.4	-17.96	40.66	iE	50
Mrk 900	14.17±0.03	13.56±0.12	0.61±0.13	55±6	-17.20	40.37	nE	68
Mrk 314	13.55±0.03	13.12±0.24	0.43±0.24	64±13	-18.99	40.90	iI,M	53
Mrk 324	15.17±0.03	14.60±0.13	0.57±0.14	16.0±1.9	-16.84	40.09	nE	51
Mrk 328	14.93±0.05	14.18±0.09	0.74±0.10	17.4±1.4	-16.82	40.02	nE	38

Note. — Columns stand for: (1) Galaxy name (2) B -band integrated magnitude and its $1\text{-}\sigma$ error. (3) R -band integrated magnitude and its $1\text{-}\sigma$ error. (4) $(B - R)$ integrated color its $1\text{-}\sigma$ error. (5) Integrated $\text{H}\alpha$ flux and error in units of 10^{-14} erg s $^{-1}$ cm $^{-2}$ (corrected for underlying stellar absorption). (6) B -band absolute magnitude. (7) $\text{H}\alpha$ luminosity in erg s $^{-1}$. (8) Morphological type according to the classification of Loose & Thuan (1986). (9) Equivalent width of $\text{H}\alpha$ in Å. Magnitudes, colors, fluxes, and luminosities are corrected for Galactic extinction but not for internal extinction.

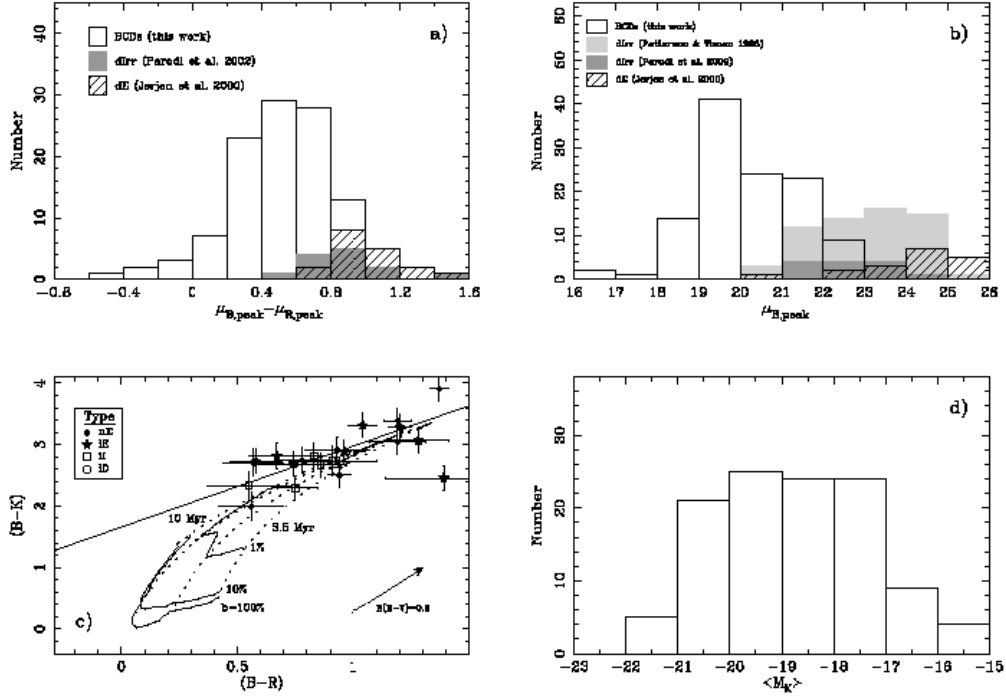


Fig. 1.— **a)** Frequency histogram of the $(B - R)$ color at the peak of the surface-brightness profile for our sample of BCD galaxies and a sample of dIrr (Parodi et al. 2002) and dE (Jerjen et al. 2000) galaxies. An average galactic-extinction correction of $A_B=0.1$ mag has been applied to the reference samples data. **b)** The same for the peak surface brightness. The values obtained for a sample of dIrr galaxies from Patterson & Thuan (1996) are also shown. **c)** $(B - K)$ - $(B - R)$ color-color diagram for the 21 galaxies in our Atlas with 2MASS K -band magnitudes available. The predictions of evolutionary synthesis models are shown (see text for details). The thick, solid-line represents the best fit to the data. **d)** Frequency histogram of derived absolute K -band magnitudes obtained applying the relation between the $(B - K)$ and $(B - R)$ colors shown in Panel **c**.

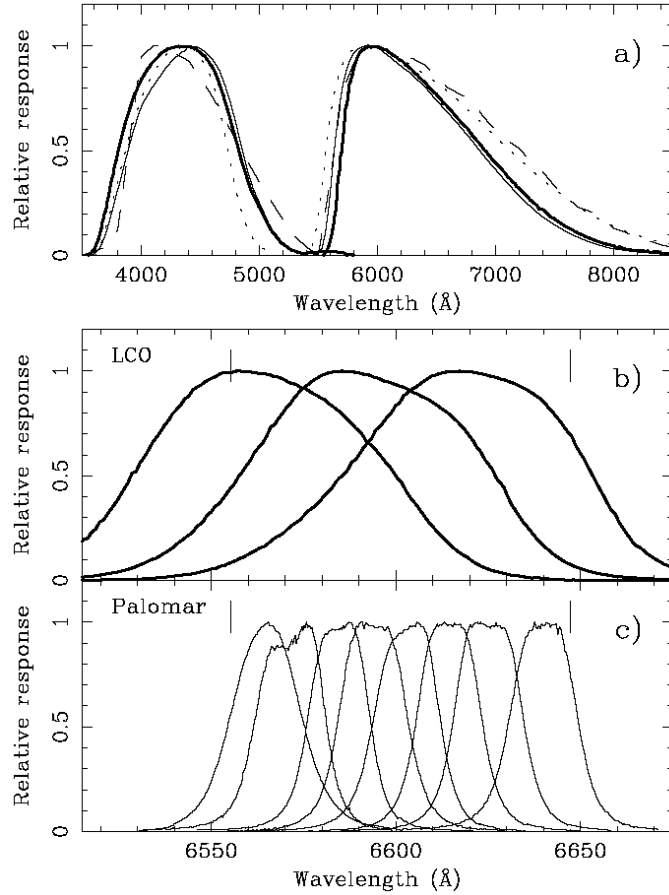


Fig. 2.— **a)** Spectral response function of the *B* and *R* broad-band filters used at the Palomar Observatory 60-inch telescope (solid-thin line) and at the Las Campanas Observatory du Pont 100-inch telescope (solid-thick line) convolved with the quantum efficiency of the detector. The response function of the filters used by Landolt (1992a; dotted-line) to construct his list of secondary standards and those originally used to define the Johnson-Cousins system (dashed-line; *B*-band: Azusienis & Straižys 1969; *R*-band: Bessell 1990). **b)** Spectral response function of the narrow-band H α filters used in the Las Campanas Observatory 100-inch telescope (from left to right: LC 6570, LC 6600, LC 6630). **c)** The same as **b)** for the Palomar Observatory 60-inch telescope (from left to right: PO 6563, PO 6570, PO 6584, PO 6593, PO 6601, PO 6614, PO 6624, PO 6640). Vertical marks indicate the range in wavelength covered by the redshifted H α line for the galaxies in our sample.

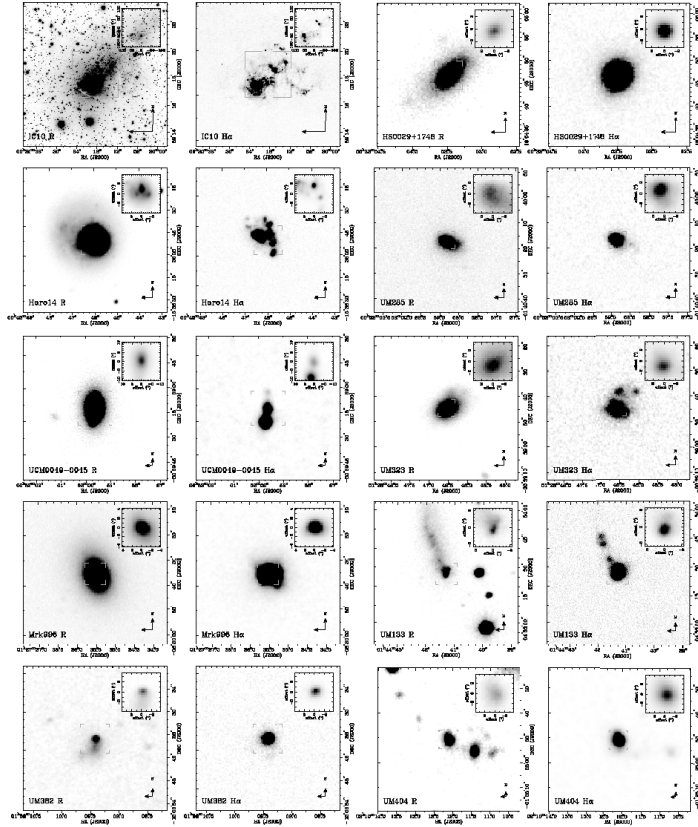


Fig. 3.— R (left) and continuum-subtracted $H\alpha$ (right) images of the galaxies in the sample. The compass is 0.5 kpc in size in each image. A blow-up image of the galaxy nuclear region is also shown.

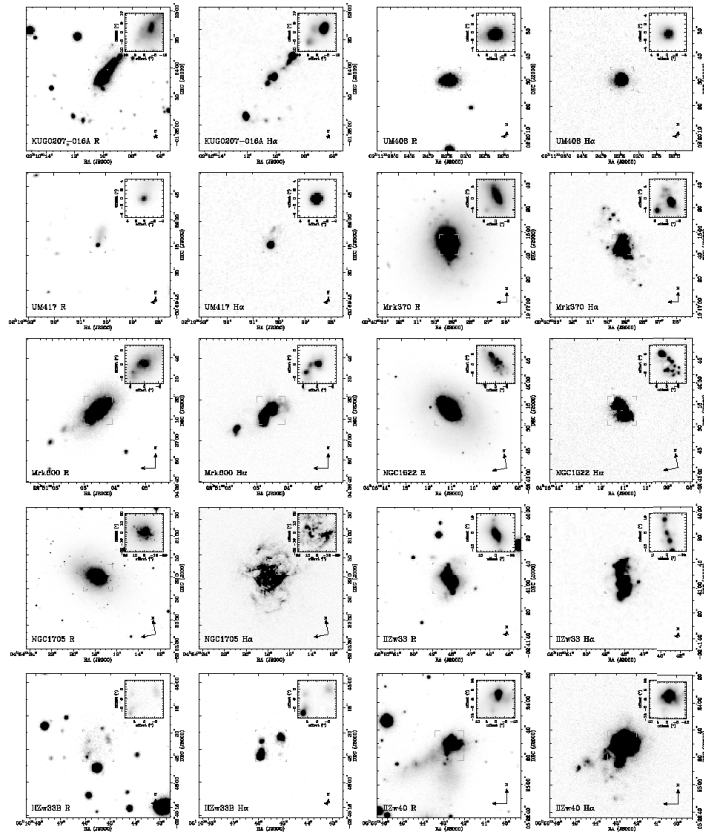


Fig. 3.— R and continuum-subtracted $H\alpha$ images of the galaxies in the sample (cont.)

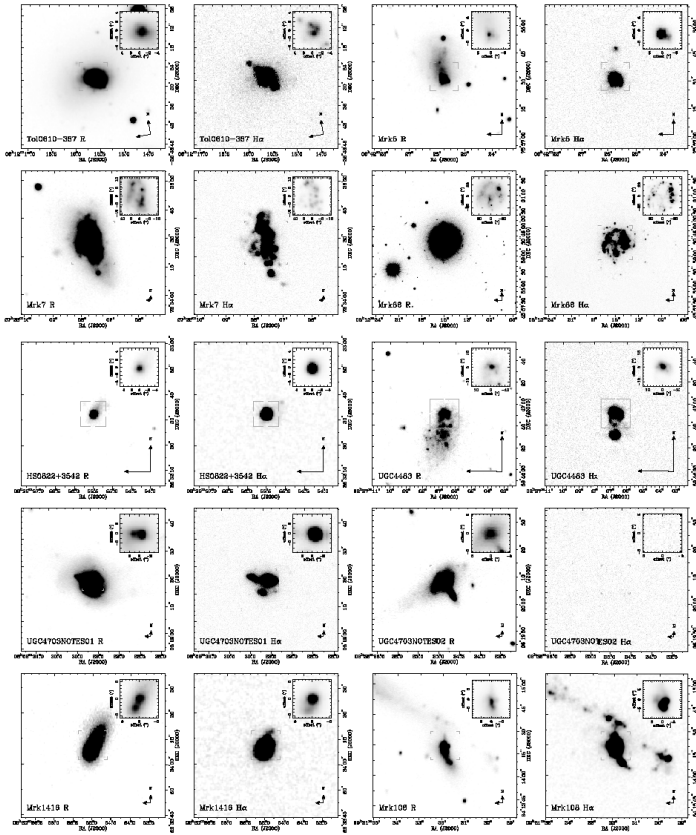


Fig. 3.— R and continuum-subtracted $H\alpha$ images of the galaxies in the sample (cont.)

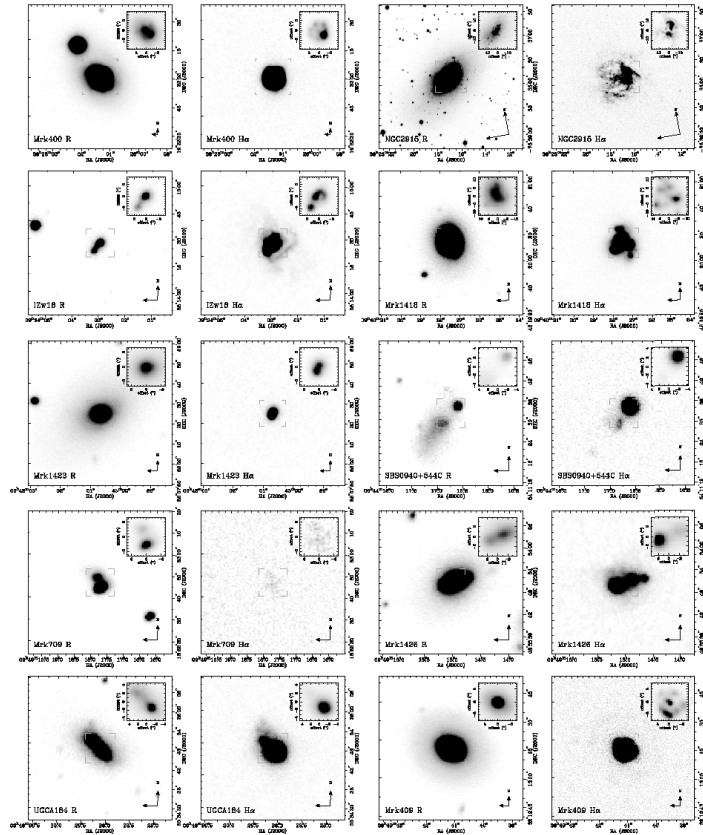


Fig. 3.— R and continuum-subtracted $H\alpha$ images of the galaxies in the sample (cont.)

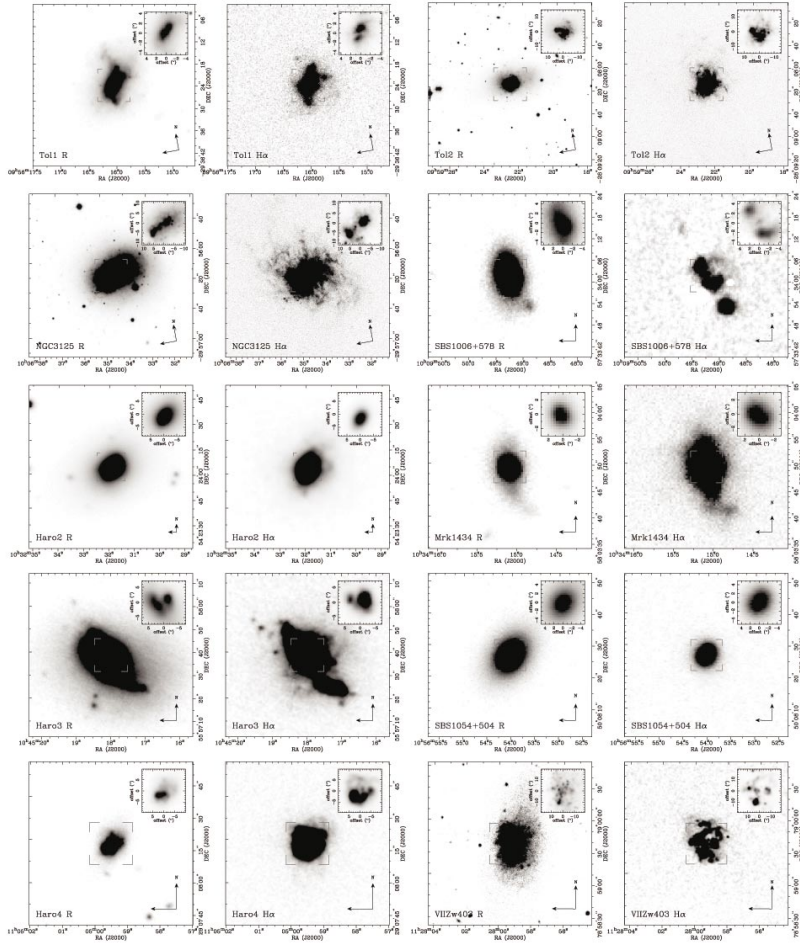


Fig. 3.— R and continuum-subtracted $H\alpha$ images of the galaxies in the sample (cont.)

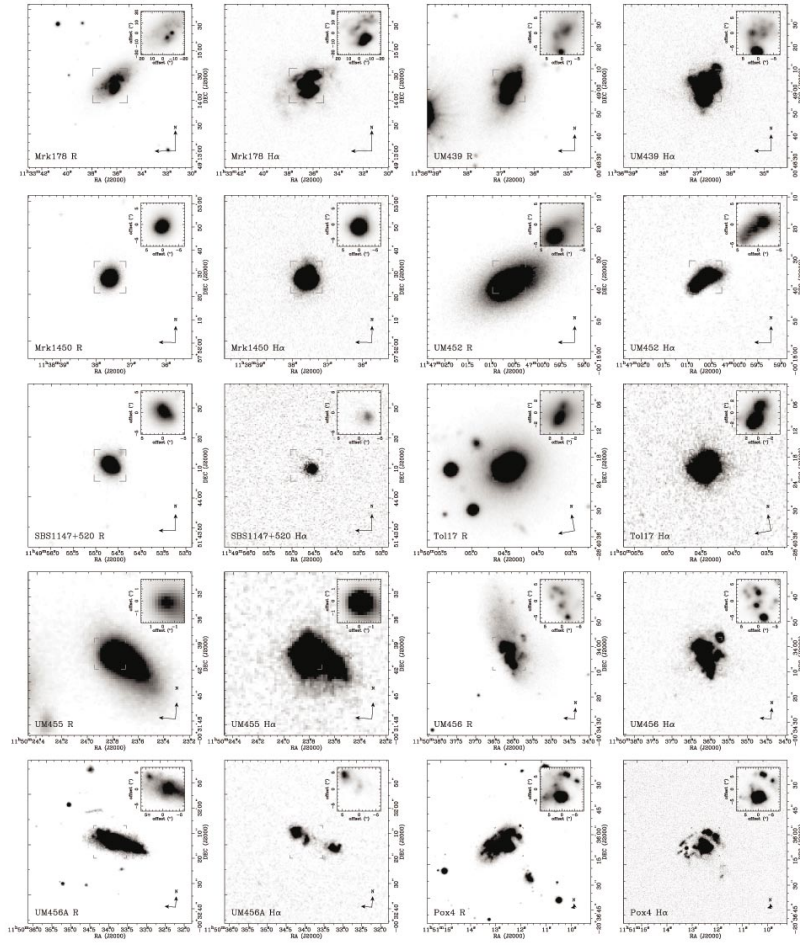


Fig. 3.— R and continuum-subtracted $H\alpha$ images of the galaxies in the sample (cont.)

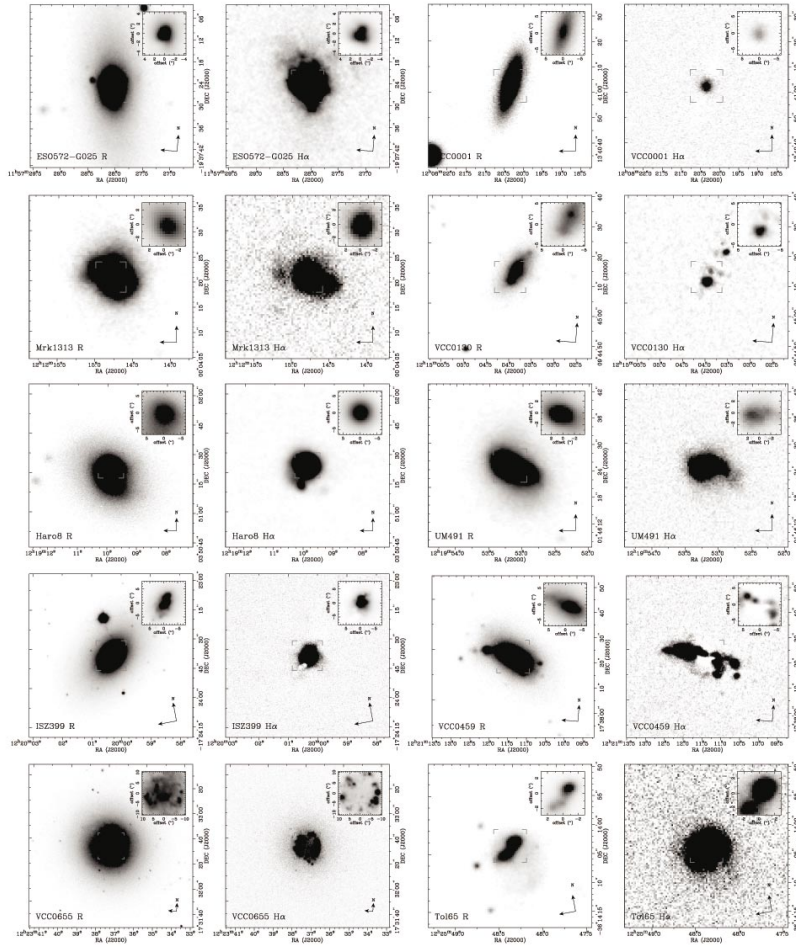


Fig. 3.— R and continuum-subtracted $H\alpha$ images of the galaxies in the sample (cont.)

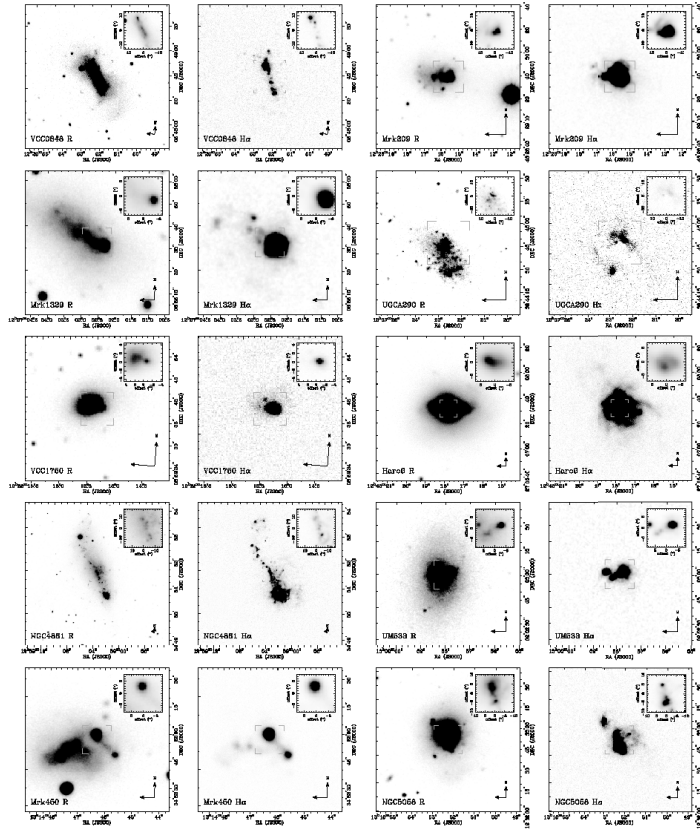


Fig. 3.— *R* and continuum-subtracted H α images of the galaxies in the sample (cont.)

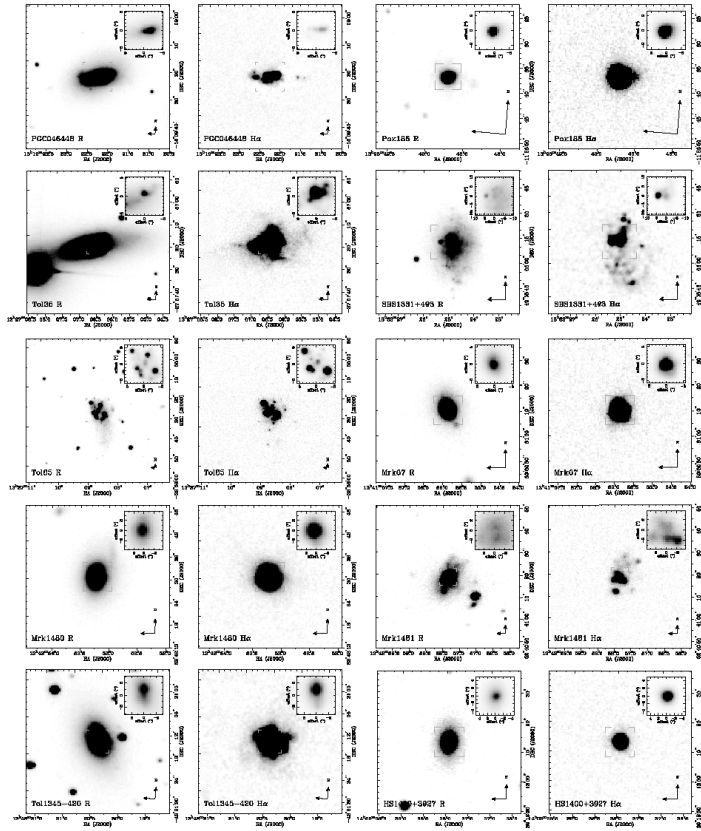


Fig. 3.— *R* and continuum-subtracted H α images of the galaxies in the sample (cont.)

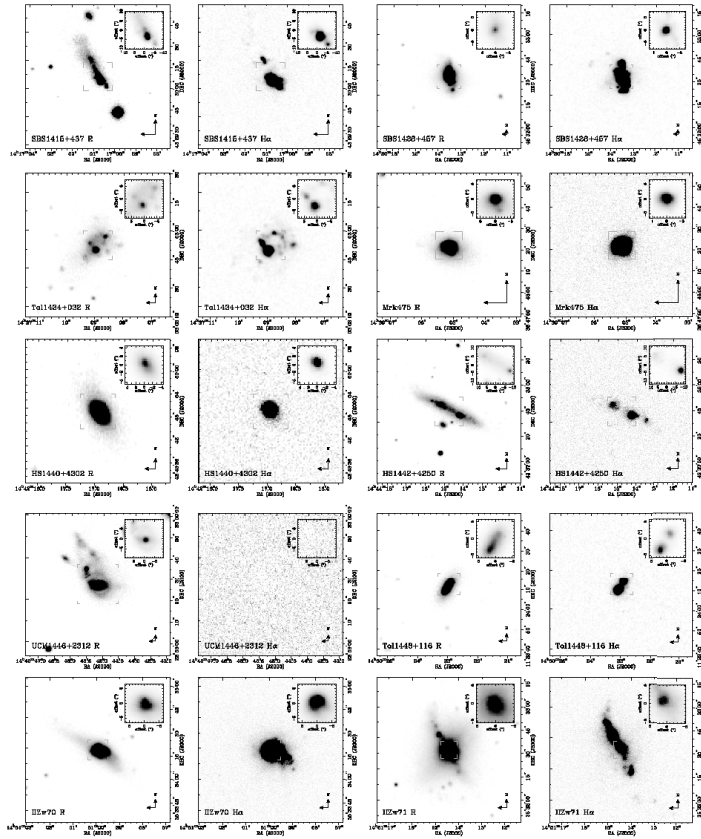


Fig. 3.— *R* and continuum-subtracted $H\alpha$ images of the galaxies in the sample (cont.)

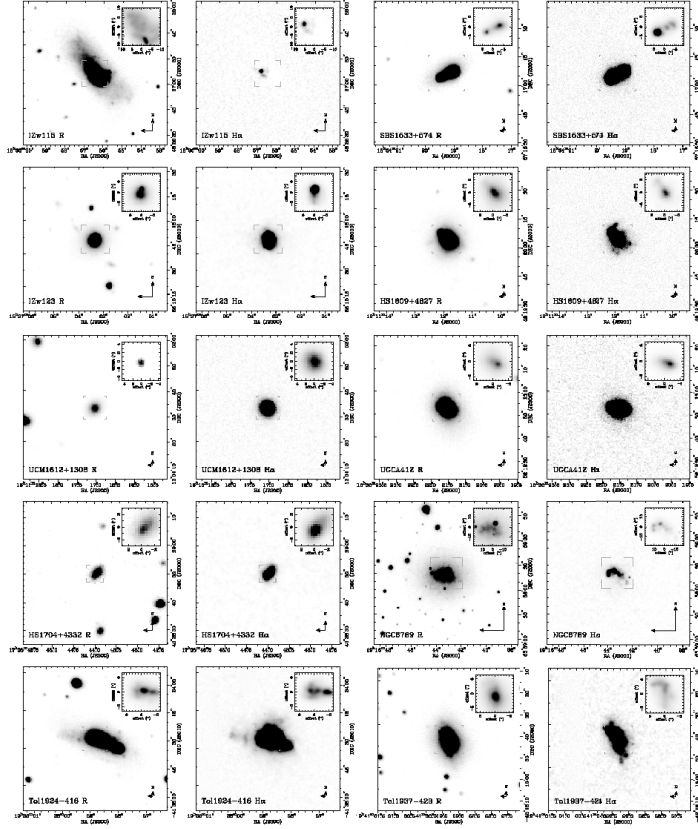


Fig. 3.— *R* and continuum-subtracted H α images of the galaxies in the sample (cont.)

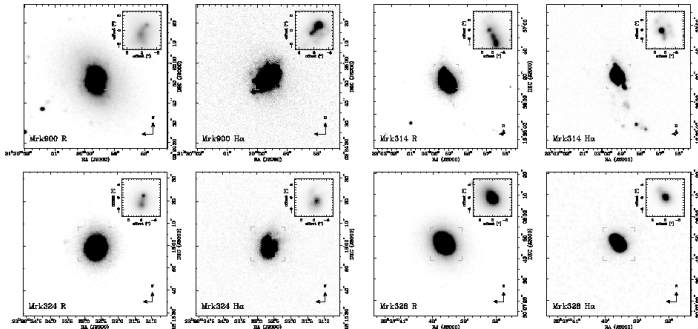


Fig. 3.— *R* and continuum-subtracted H α images of the galaxies in the sample (cont.)

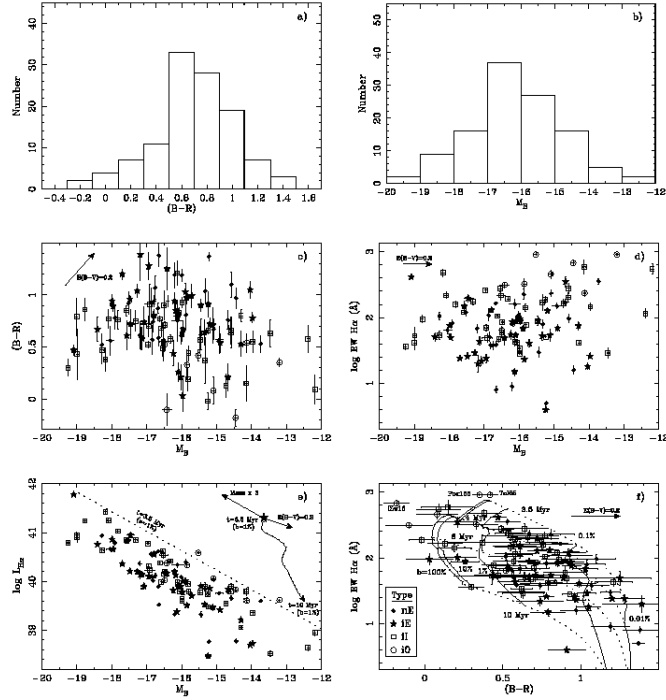


Fig. 4.— a) Frequency histogram of the $(B - R)$ color. b) Frequency histogram of the absolute magnitude, M_B . c) Color vs. M_B diagram. Different symbols are used for nE, iE, iI, and iO BCDs (see legend in Panel f). The effect of a color excess of $E(B - V)=0.2$ mag is shown by arrows. d) $\text{EW}(\text{H}\alpha)$ vs. M_B diagram. e) $\text{H}\alpha$ luminosity vs. M_B diagram. Dotted-line shows the properties of a composite stellar population formed by a 3.5-Myr-old burst with $Z_{\odot}/5$ metallicity and 1% burst strength in mass overimposed on a 9-Gyr-old underlying stellar population with the same metallicity. The effects of a change in the age of the burst, the internal extinction and total mass of the galaxy are also shown. f) $\text{EW}(\text{H}\alpha)$ vs. $(B - R)$ color diagram. The predictions of the models for the stellar population described above are shown. Solid lines represent models of constant burst strength and age between 3.5 and 10 Myr. Dotted lines are models with constant age but different burst strength.

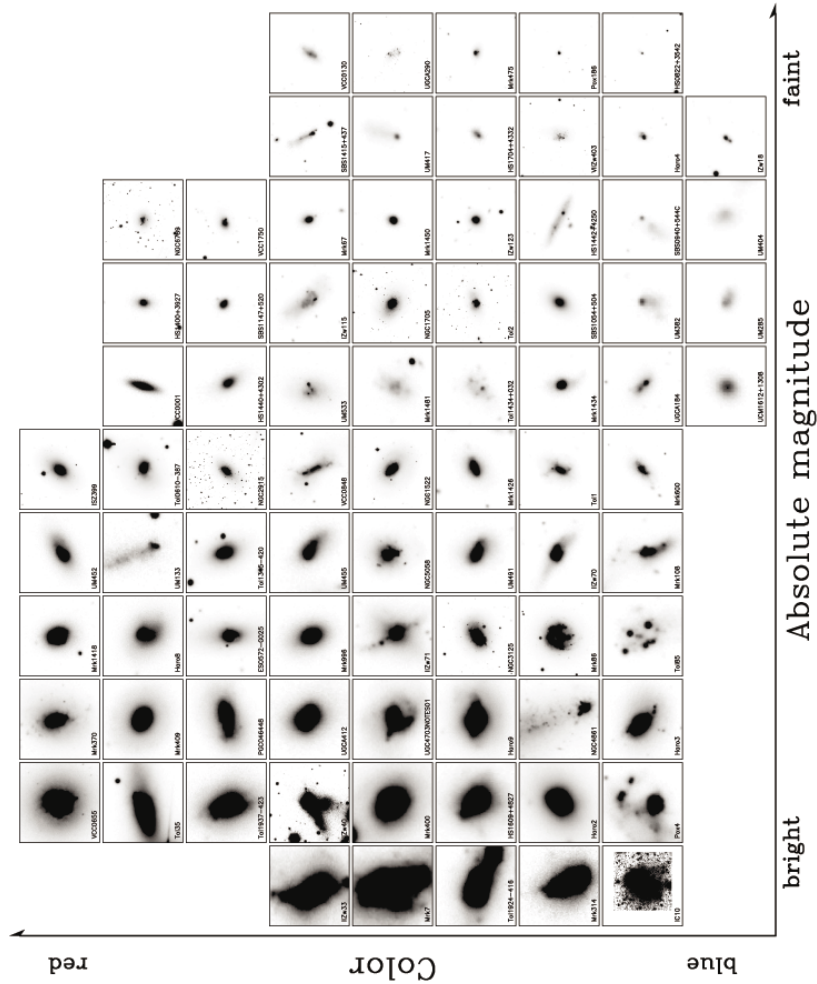


Fig. 5.— *R*-band images of 80 of the galaxies in the sample. All panels are 5 kpc in size. The grayscale ranges between the value of the sky (white) and that corresponding to a surface brightness of 21 mag arcsec⁻² (black). The name of the galaxy is shown at the bottom-left corner of each panel.

REFERENCES

- Aloisi, A., Tosi, M., & Greggio, L., 1999, *AJ* 118, 302
- Alonso, O., García-Dabó, C.E., Zamorano, J., Gallego, J., & Rego, M., 1999, *ApJS* 122, 415
- Augarde, R., Figon, P., Vanderriest, C., & Lemonnier, J.P., 1990, *A&A* 233, 348
- Azusienis, A., & Straizys, V., 1969, *Astronomicheskii Zhurnal*, 13, 316
- Bell, E.F., & de Jong, R.S., 2001, *ApJ* 550, 212
- Bessell, M.S., 1990, *PASP* 102, 1181
- Brinchmann, J., & Ellis, R.S., 2000, *ApJ* 536, L77
- Burstein, D., & Heiles, C., 1984, *ApJS* 54, 33
- Cairós, L.M., Vílchez, J.M., González-Pérez, J.N., Iglesias-Páramo, J., & Caon, N., 2001a, *ApJS* 133, 321
- Cairós, L.M., Caon, N., Vílchez, J.M., González-Pérez, Muñoz-Tuñon, C. 2001b, *ApJS* 136, 393
- Cardelli, J.A., Clayton, G.C., & Mathis, J.S., 1989, *ApJ* 345, 245
- Crone, M.M., Schulte-Ladbeck, R.E., Hopp, U., & Greggio, L., 2000, *ApJ* 545, L31
- Crone, M.M., Schulte-Ladbeck, R.E., Greggio, L., & Hopp, U., 2002, *ApJ* 567, 258
- de Vaucouleurs, G., de Vaucouleurs, A., Corwin, H.G., Jr., Buta, R.J., Paturel, G., & Fouque, P., 1991, *Third Reference Catalogue of Bright Galaxies*.
- De Young, D.S., & Heckman, T.M., 1994, *ApJ* 431, 598
- Dolphin, A.E., et al., 2001, *MNRAS* 324, 249
- Doublier, V., Comte, G., Petrosian, A., Surace, C., & Turatto, M., 1997, *A&AS* 124, 405
- Doublier, V., Caulet, A., & Comte, G., 1999, *A&AS*, 138, 213
- Doublier, V., Mas-Hesse, J.M., Caulet, A., & Kunth, D., 2001a, *A&A* 372, 22
- Doublier, V., Cualet, A., & Comte, G., 2001b, *A&A* 367, 33

- Drozdovsky, I.O., Schulte-Ladbeck, R.E., Hopp, U., Crone, M.M., & Greggio, L., 2001, *ApJ* 551, L135
- Fanelli, M., O’Connell, R.W., & Thuan, T.X., 1988, *ApJ* 334, 665
- Ferrara, A., & Tolstoy, E., 2000, *MNRAS* 313, 291
- Freedman, W.L., et al., 2001, *ApJ* 553, 47
- Gallego, J., Zamorano, J., Rego, M., Alonso, O., & Vitores, A.G., 1996, *A&AS* 120, 323
- Garnett, D.R., 1990, *ApJ* 363, 142
- Gil de Paz, A., Aragón-Salamanca, A., Gallego, J., Alonso-Herrero, A., Alonso-Herrero, A., Zamorano, J., & Kauffmann, G., 2000a, *MNRAS* 316, 357
- Gil de Paz, A., Zamorano, J., & Gallego, J., 2000b, *A&A* 361, 465
- Gil de Paz, A., Zamorano, J., Gallego, J., & Domínguez, F. de B., 2000c, *A&AS* 145, 377
- Gil de Paz, A., Silich, S.A., Madore, B.F., Sánchez Contreras, C., Zamorano, J., & Gallego, J., 2002, *ApJ* 573, L101
- González-Delgado, R.M., Leitherer, C., & Heckman, T.M., 1999, *ApJS* 125, 489
- Guseva, N.G., Izotov, Y.I., & Thuan, T.X., 2000, *ApJ* 531, 776
- Hamuy, M., Walker, A.R., Suntzeff, N.B., Gigoux, P., Heathcote, S.R., & Phillips, M.M., 1992, *PASP* 104, 533
- Haro, G., 1956, *AJ* 61, 178
- Heller, A.B., Brosch, N., Almoznino, E., van Zee, L., & Salzer, J.J., 2000, *MNRAS* 316, 569
- Hunter, D.A., 2001, *ApJ* 559, 225
- Hunter, D.A., & Hoffman, L., 1999, *AJ* 117, 2789
- Izotov, Y.I., Chaffee, F.H., & Schaerer, D., 2001a, *A&A* 378, L45
- Izotov, Y.I., et al., 2001b, *ApJ* 560, 222
- Izotov, Y.I., & Thuan, T.X., 1999, *ApJ* 511, 639
- James, P.A., 1994, *MNRAS* 269, 176

- Jansen, R.A., Fabricant, D., Franx, M., & Caldwell, N., 2000, *ApJS* 126, 331
- Jarrett, T.H., Chester, T., Cutri, R., Schneider, S., Skrutskie, M., & Huchra, J.P., 2000, *AJ* 119, 2498
- Jerjen, H., Binggeli, B., & Freeman, K.C., 2000, *AJ* 119, 593
- Kauffmann, G., White, S.D.M., & Guiderdoni, B., 1993, *MNRAS* 264, 201
- Kennicutt, R.C., 1992, *ApJ* 388, 310
- Kniazev, A.Y., Pustilnik, S.A., Ugryumov, A.V., & Pramsky, A.G., 2001, *A&A* 371, 404
- Kobulnicky, H.A., & Skillman, E.D., 1998, *ApJ* 497, 601
- Kong, X., & Cheng, F.Z., 2002, *A&A* 389, 845
- Kunth, D., Sargent, W.L.W., & Cowal, C., 1981, *A&AS* 44, 229
- Landolt, A.U., 1992a, *ApJ* 104, 340
- Landolt, A.U., 1992b, *ApJ* 104, 372
- Lauberts, A., & Valentijn, E.A., 1989, *The Surface Photometry Catalogue of the ESO-UPPSALA galaxies*. Garching bei Munchen, Germany. European Southern Observatory.
- Lee, M.G., Freedman, W.L., & Madore, B.F., 1993, *ApJ* 417, 553
- Legrand, F., Kunth, D., Roy, J.-R., Mass-Hesse, J.M., & Walsh, J.R., 2000, *A&A* 355, 891
- Loose, H.-H., & Thuan, 1986, in *Star Forming Dwarf Galaxies and Related Objects*, ed. D. Kunth, T.X. Thuan, & J.T.T. Van (Gif-sur-Yvette: Editions Frontières), 73
- Mac Alpine, G.M., & Williams, G.A., 1981, *ApJS* 45, 113
- Mac Low, M.-M., & Ferrara, A., 1999, *ApJ* 513, 142
- Macri, L.M., et al., 1999, *ApJ* 521, 155
- Markarian, B.E., Lipovetskii, V.A., & Stepanian, D.A., 1981, *Astrofizika* 17, 619
- Markarian, B.E., Stepanian, D.A., & Erastova, L.K., 1986, *Astrofizika* 25, 345
- Masegosa, J., Moles, M., & Campos-Aguilar, A., 1994, *ApJ* 420, 576

- Meurer, G.R., Carignan, C., Beaulieu, S.F., & Freeman, K.C., 1996, *AJ* 111, 1551
- Noeske, K.G., Guseva, N.G., Fricke, K.J., Izotov, Y.I., Papaderos, P., & Thuan, T.X., 2000, *A&A* 361, 33
- Östlin, G., 2000, *ApJ* 535, L99
- Papaderos, P., Loose, H.-H., Thuan, T.X., & Fricke, K.J., 1996a, *A&AS* 120, 207
- Papaderos, P., Loose, H.-H., Fricke, K.J., & Thuan, T.X., 1996b, *A&A* 314, 59
- Papaderos, P., Izotov, Y.I., Frick, K.J., Thuan, T.X., & Guseva, N.G., 1998, *A&A* 338, 43
- Papaderos, P., Izotov, Y.I., Thuan, T.X., Noeske, K.G., Fricke, K.J., Guseva, N.G., & Green, R.F., 2002, *A&A* 393, 461
- Parodi, B.R., Barazza, F.D., & Binggeli, B., 2002, *A&A* 388, 29
- Patterson, R.J., & Thuan, T.X., 1996, *ApJS* 107, 103
- Pérez-González, P.G., Gil de Paz, A., Zamorano, J., Gallego, J., Alonso-Herrero, A., & Aragón-Salamanca, A., 2003a, *MNRAS* 338, 508
- Pérez-González, P.G., Gil de Paz, A., Zamorano, J., Gallego, J., Alonso-Herrero, A., & Aragón-Salamanca, A., 2003b, *MNRAS* 338, 525
- Popescu, C.C., & Hopp, U., 2000, *A&AS* 142, 247
- Popescu, C.C., Tuffs, R.J., Völk, H.J., Pierini, D., & Madore, B.F., 2002, *ApJ* 567, 221
- Rego, M., Cordero-Gracia, M., Gallego, J., & Zamorano, J., 1998, *A&A* 330, 435
- Richer, M.G., et al., 2001, *A&A* 370, 34
- Schlegel, D.J., Finkbeiner, D.P., & Davis, M., 1998, *ApJ* 500, 525
- Schulte-Ladbeck, R.E., Hopp, U., Crone, M.M., & Greggio, L., 1999, *ApJ* 525, 709
- Schulte-Ladbeck, R.E., Hopp, U., Greggio, L., & Crone, M.M., 1999, *AJ* 118, 2705
- Schulte-Ladbeck, R.E., Hopp, U., Greggio, L., & Crone, M.M., 2000, *AJ* 120, 1713
- Schulte-Ladbeck, R.E., Hopp, U., Greggio, L., Crone, M.M., & Drozdovsky, I.O., 2001, *AJ* 121, 3007
- Salzer, J.J., 1989, *ApJ* 347, 152

- Salzer, J.J., MacAlpine G.M., Boroson, T.A., 1989, ApJS 70, 479
- Sargent, W.L.W., & Searle, L., 1970, ApJ 162, L155
- Searle, L., Sargent, W.L.W., & Bagnuolo, W.G., 1973, ApJ 179, 427
- Sharina, M.E., Karachentsev, I.D., & Tikhonov, N.A., 1999, Astronomy Letters 25, 322
- Silich, S.A., & Tenorio-Tagle, G., 2001, ApJ 552, 91
- Smith, M.G., Aguirre, C., & Zemelmann, M., 1976, ApJS 32, 217
- Steel, S.J., Smith, N., Metcalfe, L., Rabbette, M., & McBreen, B., 1996, A&A 311, 721
- Telles, E., & Terlevich, R., 1997, MNRAS 286, 183
- Terlevich, R., Melnick, J., Masegosa, J., Moles, M., & Copetti, M.V.F., 1991, A&AS 91, 285
- Thuan, T.X., & Martin, G.E., 1981, ApJ 247, 823
- Thuan, T.X., Izotov, Y.I., & Lipovetsky, V.A., 1995, ApJ 445, 108
- Thuan, T.X., Izotov, Y.I., & Foltz, C.B., 1999, ApJ 525, 105
- Tosi, M., Sabbi, E., Bellazzini, M., Aloisi, A., Greggio, L., Leitherer, C., & Montegriffo, P., 2001, AJ 122, 1271
- Ugryumov, A.V., et al., 1999, A&AS 135, 511
- Vacca, W.D., & Conti, P.S., 1992, ApJ 401, 543
- van Zee, L., Haynes, M.P., & Giovanelli, R., 1995, AJ 109, 990
- van Zee, L., Salzer, J.J., Haynes, M.P., O'Donoghue, A.A., & Balonek, T.J., 1998a, AJ 116, 2805
- van Zee, L., Skillman, E.D., & Salzer, J.J., 1998b, AJ 116, 1186
- Vanzi, L., Hunt, L.K., & Thuan, T.X., 2002, A&A 390, 481
- Vílchez, J.M., 1995, AJ 110, 1090
- Waller, W.H., 1990, PASP 102, 1217
- Walter, F., Brinks, E., Duric, N., & Klein, U., 1997, AJ 113, 2031

Zamorano, J., Rego, M., Gallego, J., Vitores, A.G., González-Riestra, R., & Rodríguez-Caderot, G., 1994, *ApJS* 95, 387

Zamorano, J., Gallego, J., Rego, M., Vitores, A.G., & Alonso, O., 1996, *ApJS* 105, 343

Zwicky, F., 1970, *Advances in Astronomy and Astrophysics*, Vol. 7. New York: Academic Press.

Zwicky, F., & Zwicky, M.A., 1971, *Catalogue of Selected Compact Galaxies and of Post-Eruptive Galaxies*. Zurich: Offsetdruck L. Speich.